Spatial-scale dependence of aerosol indirect effects over land in eastern China: A comparative analysis

Yuqin Liu[1,2], Tao Lin[1,2], Jiahua Zhang[3], Fu Wang[4], Meixia Lin[1,2], Yuan Chen[1,2], Yiyi Huang[1,2], Hongkai Geng[1,2], Xin Cao[1,2], Gerrit de Leeuw[5,6]

1 State Key Laboratory of Regional and Urban Ecology, Institute of Urban Environment, Chinese Academy of Sciences, Xiamen 361021, China
2 Fujian Key Laboratory of Digital Technology for Territorial Space Analysis and Simulation, Fuzhou 350108, China
3 Key Laboratory of Digital Earth Sciences, The Aerospace Information Research Institute, Chinese Academy of Sciences, Beijing 100094, China
4 CMA Earth System Modeling and Prediction Centre (CEMC), Beijing 100081, China
5 Royal Netherlands Meteorological Institute (KNMI), R&D Satellite Observations, 3730AE De Bilt, The Netherlands
6 State Key Laboratory of Remote Sensing and Digital Earth & Key Laboratory of Satellite Remote Sensing of Ministry of Ecology and Environment, Aerospace Information Research Institute, Chinese Academy of Sciences, Beijing 100101, China

Correspondence to: Tao Lin (tlin@iue.ac.cn); Gerrit de Leeuw (gerrit.de.leeuw@knmi.nl, ORCID: 0000-0002-1649-6333)

Abstract

The aim of this study is to reveal patterns of the sensitivity of aerosol indirect effects to spatial scales and investigate the regulatory role of the liquid water path (LWP) in aerosol-cloud interactions over land in eastern China. Using MODIS and CALIOP satellite observations, we systematically analyzed the relationships between aerosol optical depth (AOD) and cloud properties (cloud droplet effective radius, CER; cloud droplet number concentration, N_d) during two periods: 2008–2014 (period 1, high AOD) and 2015–2022 (period 2, decreasing AOD). The results show three distinct regimes of CER variation with LWP: a rapid growth regime (LWP < 55/50 g/m²), a decreasing regime (LWP = 55-135/50-100 g/m²) and a slow growth regime (LWP > 135/100 g/m²) (thresholds vary by period). The slow growth regime is not analyzed further due to limited data. The sensitivity of CER to AOD (S_{CER}) exhibited a negative correlation, with stronger sensitivity in the decreasing LWP regime than in the rapid growth regime. The spatial scale (characterized by buffer size and study area) significantly modulated these sensitivities: $|S_{CER}|$ and the positive sensitivity of N_d to AOD (S_{Nd}) both decreased with increasing spatial scale.

Optimal buffer sizes range from 6°×6° to 10°×10°: increasing with study area in period 2 but decreasing in period 1 for the decreasing LWP regime. Compared with period 1, |S_{CER}| in period 2 significantly reduced, reflecting the weakened aerosol-cloud interactions due to declining aerosol concentrations. Additionally, the optimal buffer sizes for S_{Nd} were larger in the 8°×8° and 10°×10° study areas than in 4°×4° and 6°×6° areas. This study reveals the scale-dependence of aerosol-cloud interactions, providing quantitative observational constraints for optimizing scale-aware aerosol-cloud parameterization schemes, particularly for constraining scale-dependent aerosol activation and cloud droplet autoconversion processes.

Keywords: Aerosol, Cloud, Liquid water path, Scale effect, Satellite, Eastern China

1 Introduction

Aerosol particles, depending on their chemical composition and size, can serve as cloud condensation nuclei (CCN) in liquid clouds or as ice nucleating particles (INP) in ice clouds. When CCN are activated, they can alter the microphysical properties of clouds and affect precipitation, indirectly impacting the Earth's radiative budget through aerosol-cloud interactions (aci) (Tao et al., 2012; Fan et al., 2016; Rosenfeld et al., 2019; Rao and Dey, 2020; Bellouin et al., 2020; Dagan et al., 2023). An increase in CCN concentrations results in a larger number of cloud droplets (N_d), and if the cloud liquid water path (LWP) remains constant, it leads to a reduction in the cloud droplet effective radius (CER) (Twomey, 1974; Feingold et al., 2003). The reduced CER leads to an increased reflection of solar radiation, i.e. a higher cloud albedo, and enhances radiative forcing due to aci (RFaci). The impact of increasing aerosol particle numbers on cloud properties, while maintaining a constant LWP, is commonly known as the "Twomey" effect (Twomey, 1977; Feingold, et al., 2001; Matheson et al., 2005; Koren et al., 2005; Meskhidze and Nenes, 2010; Costantino et al., 2010; 2013). Another aspect of RFaci involves quick adjustments, which could also cause changes in other cloud characteristics due to the rise in N_d and the decrease of CER. For example, this may lead to a reduction in precipitation efficiency, causing an increase in the LWP and cloud cover. As a result, the reflection of solar radiation is intensified (Albrecht, 1989). These two effects of aci are often categorized as the cloud albedo effect and the cloud lifetime effect (Quaas et al., 2008).

Extensive research on the impact of aerosols on the microphysical properties of clouds has been conducted utilizing satellite observations (Liu et al., 2017; Jia et al., 2022), aircraft measurements (Jia et al., 2019; Zheng et al., 2024), ground-based monitoring (Sarna et al., 2016; Zheng et al., 2020), and numerical simulations (Lee et al., 2025; Li et al., 2008). Among these, satellite-based instruments have become a vital observational tool for studying aci due to their wide spatial coverage and high spatiotemporal resolution. However, optical satellite sensors such as the Moderate Resolution Imaging Spectroradiometer (MODIS) cannot effectively penetrate cloud layers (King et al., 2003; Kaufman et al., 2005; Remer et al., 2005), making it difficult to directly retrieve the optical properties of aerosols underneath clouds. Currently, aerosol data are mainly obtained in cloud-free conditions as determined using cloud detection methods. This limitation results in significant spatial mismatches between aerosol and cloud properties, often requiring aggregation of satellite data over large-scale grids for statistical analysis to determine relationships between aerosol and cloud parameters. The discrepancy between this large-scale analysis and the actual process scale frequently leads to biases in quantifying aerosol indirect effects, thereby significantly increasing the uncertainty in radiative forcing estimates (Lebsock et al., 2013; Altaratz et al., 2014; Ma et al., 2015; Possner et al., 2016; Bender et al., 2018).

In recent years, studies based on multi-source satellite data or multi-instrument joint observations have demonstrated that aerosol particles significantly influence cloud microphysical properties (Saponaro et al., 2017; Liu et al., 2018; Pandey et al., 2020). Numerous studies have validated the existence of the Twomey effect (Jones et al., 2009; Christensen et al., 2016; Jia et al., 2019). However, also studies have been published with findings that contradict the Twomey effect, particularly over land, where an increase in aerosol optical depth (AOD) results in an increase in CER (Feingold et al., 2001; Yuan et al., 2008; Grandey and Stier, 2010; Tang et al., 2014; Wang et al., 2015; Ma et al., 2018; Jia et al., 2019; Liu et al., 2020). These inconsistent findings highlight the complexity and regional variability of aci mechanisms, and further in-depth research is needed to reveal the underlying processes.

Currently, researchers usually use grid methods (such as 1°× 1°, 2°× 2°, etc.) to study the aerosol indirect effects in large areas (Bréon, 2002; Kaufman et al., 2005; Bulgin et al., 2008; Quaas et al., 2008). For instance, Grandey and Stier (2010) estimated the relationship between aerosols and CER on a global scale (60°N~60°S) using multiple spatial resolutions (1°×1°, 4°×4°, 8°×8°, 15°×15°, and 60°×60°). They concluded that the sensitivity of retrieved CER to AOD generally exhibited positive values over land and negative values over oceans, and pointed out that using grids larger than 4°×4° could introduce significant errors due to the spatial variability of aerosol and cloud parameters. Additionally, the study highlighted that, when using grids larger than 4°×4° to investigate the relationship between aerosols and CER, significant errors could be introduced in calculating the aerosol indirect effect index due to the spatial variability of aerosol and cloud parameters.

For studies focusing on smaller regions, researchers often employ a moving window or a fixed area referred to as a buffer zone, within which the distribution of aerosol concentrations is assumed to be uniform. Spatially matched samples are constructed by averaging AOD and cloud parameters within the window or buffer zone. The choice of the window or buffer size is often arbitrary, and existing studies rarely systematically explore how the detection of aci signals is influenced by the size of the area. For example, Yuan et al. (2008) used a 100 km × 100 km moving window to calculate the mean values of AOD and cloud properties to investigate the relationship between aerosols and CER across seven global regions. Their results indicated that only two of these regions, near the coasts of the Gulf of Mexico and the South China Sea, exhibited a positive correlation between CER and AOD. Similarly, Jones et al. (2009) utilized multi-source remote sensing data and applied a point spread function to derive the mean AOD within a 20 km range, which was designed to match the native 20 km resolution of the corresponding cloud properties (cloud optical thickness, COT; LWP; CER; cloud top pressure, CTP). Their study examined the influence of aerosol types, cloud conditions, and atmospheric factors on aerosol indirect effects across six different oceanic regions globally, finding that the sensitivity of cloud properties to AOD varied substantially with regional characteristics. In addition, significant progress has been made in research utilizing observations from the Cloud-Aerosol Lidar with Orthogonal Polarization (CALIOP) data (Winker et al., 2007). For instance, Costantino et al. (2010) used CALIOP data to investigate the aerosol influence on CER in stratocumulus clouds over the coastal regions of Namibia and Angola. They performed the analysis by co-locating an aerosol index (based on AOD and the Ångström exponent) with CER within a 150 km buffer zone around CALIOP observations. They found that there was no correlation between aerosol load and CER when aerosol and cloud layers were clearly separated, but a strong correlation when lidar profiles indicated mixing. Costantino et al. (2013) further analyzed the statistical relationship between aerosol concentrations and cloud physical parameters by examining aerosol and cloud properties within a 20 km buffer zone around CALIOP samples, integrating vertical profiles of aerosol and cloud data. Their statistics also clearly showed that cloud micro-physical properties were affected by aerosols when aerosol and cloud layers were mixed, decreasing the CER. It is noted that these two studies by Costantino et al. (2010, 2013) reached consistent conclusions about aci (i.e., aerosols modulate CER when layers interact), by adopting different buffer sizes (150 km vs. 20 km) to target distinct study areas. This demonstrates that the buffer size is tailored to the research objectives rather than through a systematic sensitivity analysis. Wang et al. (2015) revealed an inverse “Twomey” effect between aerosols and CER in eastern China by analyzing aerosol concentrations and CER within a 50 km buffer zone around CALIOP samples. Their results showed that larger CER was associated with high AOD, which was attributed to the feedback of microphysical processes from intense competition for vapor in the presence of high aerosol concentrations and the evaporation of smaller, less hygroscopic, droplets. Similarly, Liu et al. (2017) systematically examined the response mechanisms of warm cloud macro- and microphysical parameters to increasing AOD in the Yangtze River Delta region, also using CALIOP samples within a 50 km buffer zone. They found that the relation between cloud properties and AOD depended on the aerosol abundance, with a different behavior for low and high AOD (i.e. $AOD < 0.35$ and $AOD > 0.35$). However, both Wang et al. (2015) and Liu et al. (2017) used a fixed 50 km buffer zone without justifying the choice or exploring how varying buffer sizes might alter the strength or robustness of their findings—a common limitation in regional aci studies. More recently, Liu et al. (2024) quantified the relative importance of aerosols, meteorological parameters and their interactions for cloud properties in the eastern coastal and inland regions of China, utilizing MODIS 1°×1° aerosol and cloud product data. Their study confirmed that CER decreased with the increase in AOD in the moderately polluted atmosphere ($0.1 < AOD < 0.3$) over the East China Sea, whereas, in contrast, CER increased with increasing AOD in the polluted atmosphere ($AOD > 0.3$) over the Yangtze River Delta. These studies have provided critical scientific insights into aci at regional scales, but the lack of systematic scale sensitivity analysis—especially for varying window/buffer sizes within the same regional domain—leaves uncertainties about the generalizability of their conclusions.

However, the properties and interaction processes of aerosols and clouds are spatially significantly heterogeneous and scale dependent (McComiskey et al., 2009; McComiskey and Feingold, 2012; Chen et al., 2015; Glotfelty et al., 2020). McComiskey and Feingold (2012) explicitly pointed out that the “scale problem” is a major challenge in quantifying aerosol indirect effects, as the spatial scale of observation can mask or exaggerate the true interaction signals. In previous studies, the definitions of window size and buffer size have often been subjective, inadvertently introducing uncertainties into the research on aci. Although studies have explored the relationship between aerosols and CER across different observational scales, these investigations have primarily focused on larger spatial scales, leaving a gap in sensitivity analysis of aerosol indirect effects at smaller regional scales. For example, Grandey and Stier (2010) focused on global-scale grid resolutions but did not explore the scale dependence within regional domains; Wang et al. (2015) and Liu et al. (2017) used fixed buffer sizes (50 km) without investigating how varying buffer sizes affect the results. Therefore, identifying the spatial scale dependence of the aerosol indirect effect over eastern China provides observationally based coefficients. These coefficients can be used to develop regionally adapted, scale-aware parameterization schemes that better represent regional ACI characteristics.

Aerosol properties in China have significantly changed between 2008 and 2022 due to economic development and the implementation of emission reduction policies. The AOD over China increased until 2007 to become among the highest worldwide and remained high between 2008 and 2014 with large interannual variations. The enforcement of emission reduction measures, in particular the implementation of the 2013-2017 Clean Air Action Plan, resulted in the decline of the AOD between 2014 and 2018 (de Leeuw et al., 2021; 2022; 2023) and a further decrease resulted in an AOD lower than that in 2000 (de Leeuw et al, 2023). This distinct two-period variation (high AOD vs. decreasing AOD) provides a unique opportunity to investigate how changes in aerosol loading modulate the scale dependence of aerosol indirect effects, a topic that has not been systematically addressed in previous studies. Based on these observations, in this study we conduct a comparative analysis of the sensitivity of cloud parameters (CER and N_d) to AOD variation using data from two distinct periods: 2008-2014 (period 1, high AOD) and 2015-2022 (period 2, decreasing AOD). The main objectives of this study are to: (1) reveal patterns of the sensitivity of aerosol indirect effects to spatial scales by investigating how spatial scale modulates the sensitivity of CER to AOD (S_{CER}) and the sensitivity of N_d to AOD (S_{Nd}) over eastern China during the two periods; and (2) clarify the regulatory role of LWP in aci by examining the LWP-stratified responses of S_{CER} and S_{Nd} to spatial scale and AOD variations. This study reveals the spatial scale-dependent sensitivity of aerosol indirect effects, supporting the development of scale-adaptable parameterization modules and improved regional aerosol effect assessment under different model grid resolutions.

2 Method

2.1 Study area

Eastern China (30°N-40°N, 112°E-122°E; Figure 1) has undergone remarkable economic expansion over the past three decades, which was accompanied by a substantial increase in AOD. Eastern China presents a unique atmospheric laboratory due to its complex aerosol composition - featuring both anthropogenic pollutants from industrial emissions and natural mineral dust transported from Central Asian deserts, particularly during the spring (Proestakis et al., 2018; Liu et al., 2021). The multitude of sources and the persistent nature of these aerosol particles, which can remain suspended for days to weeks and be transported over long distances in the absence of precipitation (Costantino et al., 2013; Li et al., 2021; Leung et al., 2023), makes eastern China an ideal study area for investigating aci. Our research leverages satellite observations to systematically evaluate the sensitivity of cloud properties (S_{CER} and S_{Nd}) to the AOD variation, thereby revealing the scale-sensitive patterns of aerosol indirect effects and clarifying the regulatory role of LWP in aci over this region.

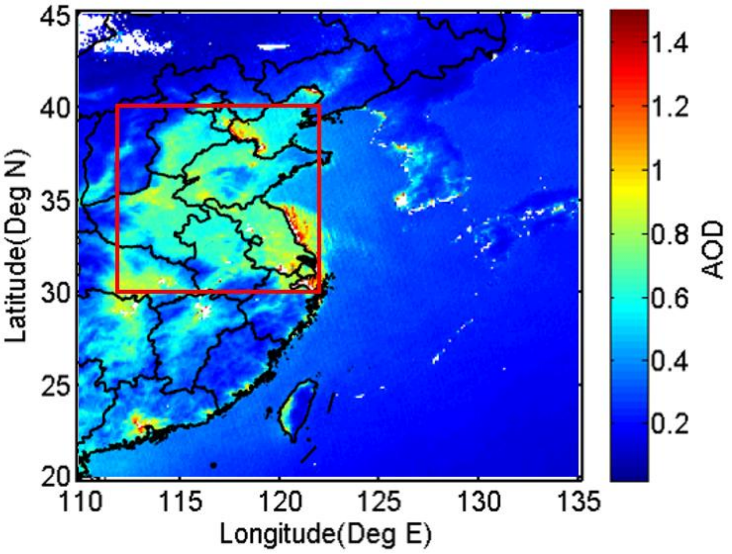

Figure 1. Map of annual averaged MODIS/AQUA level 2 AOD for all years during the period from 2008 to 2022. The red rectangle (30°–40°N, 112°–122°E) indicates the study area.

2.2 Data used

Data used in this study were acquired by the MODIS instrument aboard NASA's Aqua satellite, which features an extensive swath width of approximately 2300 km and comprehensive spectral coverage across multiple bands (King et al., 2003). The satellite's equator crossing time is 13:30 (Local time, i.e. in the early afternoon, coinciding with optimal development conditions for continental warm cloud systems (Wang et al., 2014; Liu et al., 2024). For aerosol characterization, we utilized the MODIS Collection 6.1 aerosol product (MOD04), generated from cloud-screened pixels with a native resolution of 500 m at nadir and subsequently aggregated to 10 km grid cells (Remer et al., 2005; Levy et al., 2010). AOD retrieval over land uses radiances measured at the top of the atmosphere (TOA) at wavelengths of 0.47, 0.66, and 2.13 μm (Remer et al., 2005). The MODIS AOD (at 550 nm) Level 2 product (10 km × 10 km) has been validated against ground-based remote sensing data and the results show that 69.40% of the MODIS AOD data fall within the expected uncertainty of ± (0.05 + 15 %) over land (Levy et al., 2013). In this study, AOD larger than 1.5 was excluded from further analysis to mitigate potential retrieval overestimation. This threshold was selected based on two key considerations: (1) Christensen et al. (2017) used MOD06 C6 data (1 km × 1 km) and reported that "large aerosol optical depths remain in the MODIS-observed pixels near cloud edges, due primarily to 3D effects (Varnái and Marshak, 2009) and the swelling of aerosols by higher relative humidity"; (2) the threshold of 1.5 aligns with widely adopted thresholds in regional aci studies over eastern China, where high AOD often coincides with complex surface conditions (e.g., urbanization, heterogeneous land cover) that exacerbate retrieval biases (Wang et al., 2015; Liu et al., 2017, 2021).

The cloud properties used in this study, including CER, LWP, COT, CTP, and cloud phase infrared (CPI) index, were derived from the Collection 6.1 MODIS Level 2 cloud product (MYD06) (King et al., 2003). The retrieval of these cloud characteristics utilizes six spectral channels spanning wavelengths from the visible to the near-infrared (0.66, 0.86, 1.24, 1.64, 2.12, and 3.75 μm) as described by King et al. (1997). Uncertainties in the MODIS C6.1 cloud parameters over land originate from instrument calibration, atmospheric correction, land surface properties, and model assumptions (Platnick et al., 2017, 2018). For COT, these include scene-dependent Level 1B data errors (1.5%–30%), land surface albedo errors (±15%), and atmospheric correction errors (±20%). The C6.1 algorithm addresses some prior limitations by inheriting C6's optimized lookup table design, which reduces interpolation errors to 0.1%–0.2% for near-nadir views and corrects C5's overestimation of thin-cloud COT (Platnick et al., 2017). CER uncertainties, stemming from solar irradiance error (~4% at 3.7 μm), atmospheric correction, and scattering differences, are mitigated as C6.1 retains C6's separate multi-band reporting, thereby eliminating C5's systematic bias (Platnick et al., 2017). LWP uncertainty is linked to COT/CER retrieval errors and cloud-phase classification accuracy; the latter is improved by C6's voting-based phase algorithm (preserved in C6.1), which reduces misclassification over complex surfaces like vegetation and deserts (Marchant et al., 2015; Platnick et al., 2017). For CTP (1 km resolution), uncertainties from viewing angles and cloud structure are partially countered in C6.1 by assigning fill values when the 1 km retrieval fails, avoiding surface parameter defaults. For land clouds above 3 km, CTP accuracy reaches ~50 hPa (Baum et al., 2012). Finally, CPI adopts C6's weighted voting logic (replacing C5's sequential tree), with C6.1 maintaining an enhanced Phase Agreement Fraction against CALIOP/POLDER data, which reduces uncertainties from weak thin-cloud signals and complex land interference (Marchant et al., 2015; Platnick et al., 2017).

Following the methodology of Platnick et al. (2017), CER and COT measurements at 3.7 μm were used to estimate N_d through adiabatic approximation principles (Quaas et al., 2006). Previous investigations have demonstrated that implementing filters based on cloud adiabaticity produced minimal effects on S_{Nd} estimates while significantly reducing the available dataset by up to 63.00% (Gryspeerdt et al., 2022). Therefore, such filtering procedures were not adopted in the current analysis. Instead, N_d calculations are initially performed at the native pixel resolution (approximately 1 km) prior to spatial aggregation, thereby avoiding potential biases associated with deriving N_d from nonlinear combinations of CER and COT at coarser resolutions (Feingold et al., 2022). To maintain data quality, the analysis incorporated several quality control measures: only single-phase liquid clouds (CPI = 1) with CTP exceeding 700 hPa and LWP smaller than 200 g m^{-2} are considered, consistent with the typical atmospheric distribution of aerosols in the lower troposphere (Michibata et al., 2014). Pixels with CER values smaller than 4 μm or COT values smaller than 4 were excluded due to increased retrieval uncertainties (Sourdeval et al., 2016). Additionally, observations were restricted to solar zenith angles <65.00° and sensor zenith angles <41.40°. This constraint was intended to reduce the influence of well-documented biases, as elaborated in Grosvenor et al. (2018).

CALIPSO (Cloud-Aerosol Lidar and Infrared Pathfinder Satellite Observations) operates within the A-Train constellation alongside the Aqua satellite and other NASA Earth-observing platforms. The primary instrument aboard CALIPSO is the Cloud-Aerosol Lidar with Orthogonal Polarization (CALIOP). CALIOP is a two-wavelength, polarization-sensitive lidar specifically designed to provide high-resolution vertical profiles of aerosols and clouds on a global scale (Winker et al., 2009). The mission and its lidar instrument are described in Winker et al. (2009), and the associated Level 1 data products are detailed in Winker et al. (2010). This advanced sensor features an exceptionally narrow ground footprint of 70 m diameter for each laser pulse. The vertical resolution of CALIOP's products varies with altitude: 30 m within 0-8.2 km, 60 m between 8.2-20.2 km, and 180 m from 20.2-30.1 km, while maintaining a consistent 5 km horizontal resolution along the track direction (Liu et al., 2009).

The coordinated A-Train configuration ensures near-simultaneous observations (within 1-2 minutes) between MODIS/Aqua and CALIOP/CALIPSO for identical atmospheric targets (Stephens et al., 2002). This temporal synchronization guarantees data consistency when extracting coincident measurements, avoiding interferences such as aerosol diffusion and cloud evolution caused by observational time lags—an advantage unparalleled by positioning methods like random grid points and ground-based stations. For spatial compatibility, we resampled the higher-resolution MODIS cloud products (CER, LWP, and N_d at 1 km native resolution) to match CALIOP's 5 km along-track scale, while directly utilizing the 5 km-resolution CTP and CPI parameters. In cases where CALIOP detected aerosol presence, we computed spatial averages of MODIS aerosol and cloud retrieval products across multiple observation scales (detailed in Section 2.4) centred on CALIOP targets. This approach assumes reasonable homogeneity of aerosol properties between adjacent clear and cloudy regions (Anderson et al., 2003; Quaas et al., 2008). Table 1 provides a comprehensive overview of the aerosol and cloud datasets including the parameters used from each product, the resolution, and the data source, used in this study.

Table 1. Aerosol and cloud products, parameters, horizonal resolutions, and their sources applied in the present study.

Product	Parameters	Horizontal resolution	Data source
Aerosol (MYD04 Level 2 Collection 6)	Latitude	10 km	MODIS
	Longitude	10 km	
	Scan_Start_Time	10 km	
	AOD at 550 nm	10 km	
Cloud (MYD06 Level 2 Collection 6)	Latitude	5 km	
	Longitude	5 km	
	Scan_Start_Time	5 km	
	CER at 3.7 um and 2.1 um	1 km	
	LWP at 3.7 um	1 km	
	COT at 3.7 um	1 km	
	Cloud multi-layer flag	1 km	
	Cloud_Phase_Infrared_Day	5 km	
	Cloud_TOP_Pressure_Day	5 km	
	Sensor_Zenith_Day	5 km	
	Solar_Zenith_Day	5 km	
Aerosol (05kmALay)	Latitude	5 km	CALIOP
	Longitude	5 km	
	Profile_Time	5 km	

2.3 Calculation of sensitivities

Variations in aerosol loading significantly influence cloud optical properties (such as COT) and microphysical parameters (such as CER). Under specific environmental conditions, aerosol particles can transform into CCN or INP, a process primarily determined by their chemical composition and ambient temperature (Bellouin et al., 2020). When these nuclei are activated, water vapor condenses on their surfaces to form cloud droplets or ice particles. As the concentration of aerosol particles increases, the number of CCN or INP may rise correspondingly, leading to an increase in the number of cloud droplets. Notably, under conditions where the liquid water content in clouds remains constant (i.e., LWP), the same amount of water vapor is distributed across more cloud droplets, resulting in a reduction in the size of individual droplets. Specifically, as aerosol concentration increases, the CER decreases, while cloud albedo increases. On the basis of findings of Kaufman and Fraser (1997), Feingold et al. (2001) pointed out that the sensitivity of cloud microphysical properties (e.g., CER) to changes in the number concentration of aerosol particles (e.g., using AOD as a measure) can be described by the following formula:

$$\mathrm{S_{CER}}= \frac{d\,ln\,r_e}{d\,ln\,\alpha}\Big|_{\mathrm{LWP}} \quad -0.33 < \mathrm{S} < 0 \qquad (1)$$

Where r_e represents the CER and α represents the AOD. Following Andreae (2009), AOD and CCN are correlated and AOD varies with CCN following a power law relationship. Eq. (1) describes the relative change of CER with the relative change of the AOD for constant LWP. It is noted that this formulation differs from that used in recent studies (e.g., Bellouin et al., 2020) where S is expressed in terms of N_d with no restriction in LWP. The sensitivity S of CER to AOD can be determined as the slope of a linear fit to a log-log plot of CER versus AOD. The effect of aerosols on CER is analyzed by comparing the difference in $\mathrm{S_{CER}}$ and correlation coefficients between AOD and CER under different spatial scales (Section 2.4) and LWPs (Section 3.2).

In this study, the variation in N_d with CCN is referred to as the susceptibility S_{Nd}. Following the method of Gryspeerdt et al. (2023), the sensitivity, S_{Nd}, of a cloud property, N_d, to α is defined here as

$$S_{Nd} = d \ln N_d \,/\, d \ln \alpha \qquad 0 < \mathrm{S} < 1 \qquad (2)$$

Relations between CER and N_d and AOD are determined through Eq. 1 and Eq. 2 and correlation coefficients R. The significance of these relations is determined by using the student’s t test, i.e. the results are statistically significant when the p value is smaller than 0.01, where p is defined as the probability of obtaining a result equal to or “more extreme” than what was actually observed.

This method quantifies the sensitivity of CER and N_d to AOD variations via linear regression in log-log space, using Eq. 1 and Eq. 2, respectively. Its core assumptions, uncertainties, and limitations are highly consistent: both rely on AOD as an aerosol proxy variable, assume constant cloud liquid water content and a linear sensitivity relationship, and depend on the reliability of satellite-retrieved parameters (Feingold et al., 2001; Gryspeerdt et al., 2023). However, AOD cannot distinguish aerosol size and hygroscopicity, retrieval errors are substantial in clean conditions, and linear fitting fails to capture nonlinear/non-monotonic responses. Both methods are constrained by satellite retrieval biases, limited scenario applicability (only valid for specific homogeneous clouds and aerosol types), the omission of key modulating factors (dynamical conditions, aerosol type) and feedback processes, and can only assess first-order direct effects. Reliability requires scenario constraints and uncertainty analysis; the only nuances come from the target variable (CER vs. N_d), which do not alter the shared methodological limitations.

2.4 Research design for scale effects analysis

This study was conducted at multiple spatial scales to examine the scale dependence of S_{CER} and S_{Nd} in delineating aci (Fig. 2). Here, the spatial scales are described by two parameters: study area size (the geographic scope of the analysis) and buffer size (the local spatial extent around each observation point for aggregating aerosol and cloud data). To this end, the study area was divided into four congruent square research areas all centered at the same geographical location (35°N, 117°E) over Eastern China. Hence, spatial extent varies from the whole study area as defined in Section 2.1 (30°N-40°N, 112°E-122°E) to successively smaller areas simulated by decreasing the study area in steps of 2° to 4°×4° as illustrated in Figure 2a.

Buffer size refers here to a circular spatial domain centered at each point in the study area where CALIOP detected the presence of aerosols. Within this circular domain, MODIS-retrieved cloud and aerosol data (AOD, CER, N_d, LWP) are spatially averaged to construct matched aerosol-cloud datasets at different local scales. As previously noted, this approach relies on the assumption that aerosol properties are reasonably homogeneous between adjacent clear and cloudy regions (Anderson et al., 2003; Quaas et al., 2008), and this premise is supported by the short-range transport of aerosols (e.g., 10–300 km) and the near-simultaneous observations (1–2 minutes) by MODIS and CALIOP within the A-Train constellation. Buffer zones with sizes increasing from 10 to 300 km (10, 20, 30, 40, 50, 60, 70, 80, 90, 100, 120, 140, 150, 160, 180, 200, 250, and 300 km) were determined within the whole study area by using CALIOP data. Previous observations indicate that the typical horizontal scale of cloud clusters ranges from tens to hundreds of kilometers (Zhang et al., 2024; Cai et al., 2022), supported by CloudSat/CALIPSO satellite data showing power-law distributed cloud scales (10-1000 km fitting range) covering major cloud types (Zhang et al., 2024) and regional evidence of consistent multi-season, multi-latitude cloud extents (Cai et al., 2022). Meanwhile, aerosol spatial homogeneity varies with distance: local-scale aerosols ($\leq$ 50 km) exhibit high homogeneity due to consistent sources and stable diffusion, while regional-scale aerosols (> 100 km) show enhanced heterogeneity from multi-source mixing and atmospheric transport (Hassan et al., 2024; Mohebalhojeh et al., 2026). Thus, the 10–300 km buffer range covers both cloud characteristic scales and the aerosol homogeneity transition range, ensuring that MODIS data averaging effectively captures aci. This range avoids insufficient MODIS pixel coverage due to excessively small buffer sizes (< 10 km). It also prevents conflation between regional meteorological variations and local aci signals arising from overly large buffer sizes (> 300 km), as synoptic-scale circulation and other regional meteorological changes may interfere with local aci signals (Quaas et al., 2010). Meanwhile, this range aligns with the 50 – 150 km buffer sizes widely adopted in regional aci studies (Wang et al., 2015; Liu et al., 2017; 2024), enabling cross-validation of results and ensuring that MODIS data averaging effectively captures aci.

MODIS-retrieved cloud and aerosol data were averaged over a buffer area around each CALIOP data point with a radius varying from 10 to 300 km. Thus, a dataset including aerosol and cloud properties was constructed with different buffer sizes. The effect of buffer size on the sensitivity of CER and N_d to variations in AOD was determined in each study area varying from 4°×4° to 10°×10°. To this end, for each buffer size, the averaged AOD and cloud parameters were paired to calculate the sensitivities S_{CER} (Eq. 1) and S_{Nd} (Eq. 2), as well as their correlation coefficients (R) between cloud properties (e.g., CER, N_d) and AOD. The optimal buffer size for each study area is defined as the one maximizing the R. This definition is adopted based on two core considerations. Firstly, it aligns with the statistical principle that a higher R value indicates a stronger linear correlation between the two variables in log-log space, minimizing the interference of random noise and non-aerosol confounding factors on the sensitivity estimation (Quaas et al., 2006; Gryspeerdt et al., 2022). This ensures that the derived S_{CER} can reliably reflect the intrinsic relationship between aerosol loading and cloud droplet effective radius, rather than spurious correlations caused by inappropriate spatial scales. Secondly, this definition also facilitates comparability with existing literature, as it aligns with the methodological framework of satellite-based aci studies (Saponaro et al., 2017; Liu et al., 2021). In these studies, the optimal spatial scale is typically identified by maximizing the statistical robustness of variable correlations.

The dataset was used to study the characteristics of aerosol indirect effects as function of buffer size and study area, for two different periods: one with a high aerosol content (2008-2014) and another one with a decreasing aerosol content (2015-2022). This approach determined the optimal buffer size for aerosol indirect effect estimations as a function of study domain size, providing key observational constraints for constructing scale-adaptive parameterization frameworks suitable for different domain sizes over eastern China.

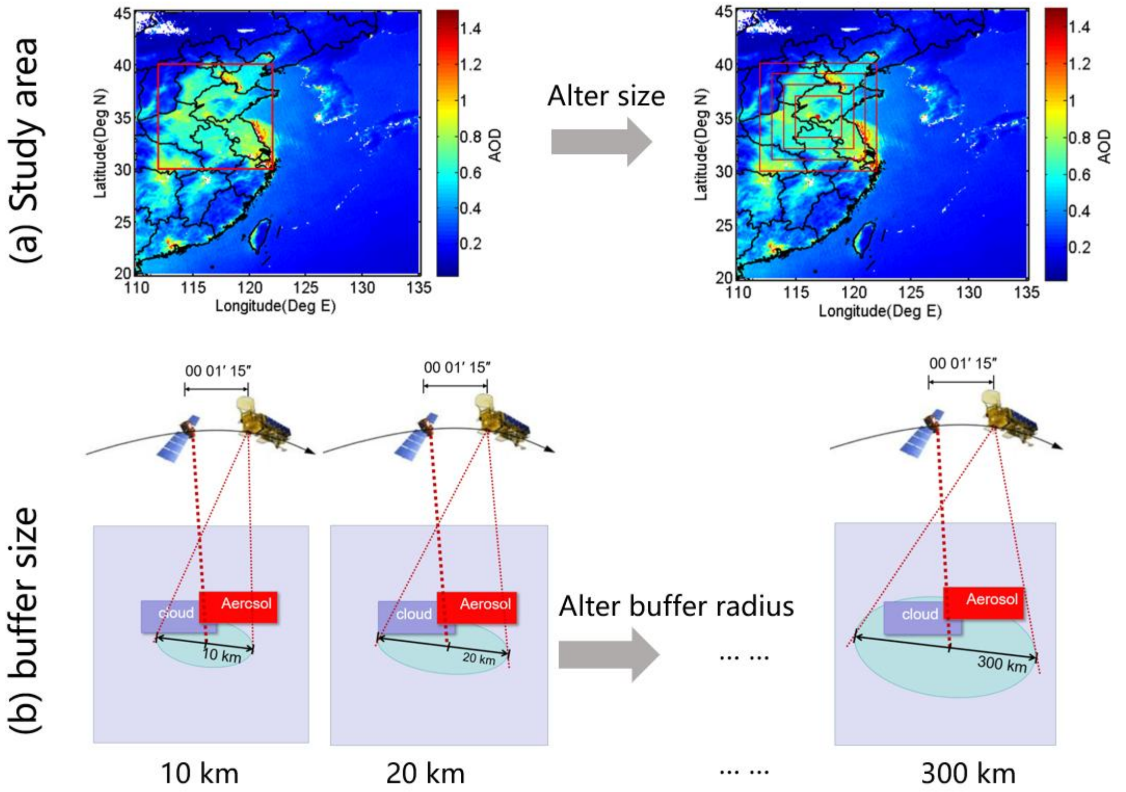

Figure 2. (a) Schematic diagram of study area and buffer size patterns applied in this study. (b) scheme of CALIPSO-MODIS coincidence methodology. When CALIPSO detects the presence of aerosol and cloud fields, we look for MODIS retrievals within a buffer size from the CALIPSO target. The temporal coincidence is insured by the coordinated satellite orbits.

3 Results

3.1 Spatial variations of aerosol and cloud parameters

Figure 3 illustrates the spatial distributions of AOD and cloud properties (CER and N_d) across the study region, averaged for the periods 2008-2014 and 2015-2022. The AOD spatial patterns (Fig. 3a,d) show similar spatial distributions during both periods, but with notably reduced values during the latter. Pronounced spatial gradients in AOD are evident during both periods. The lowest AOD values occur over the mountainous regions of Shanxi province in the northwest, while elevated concentrations appear in the southeastern areas encompassing the Hebei and Shandong provinces. This geographical contrast arises from the mountain ranges that demarcate the heavily industrialized, densely populated North China Plain (NCP) in the east - characterized by substantial anthropogenic emissions - from the relatively cleaner western regions. Under prevailing southeasterly wind conditions, these topographic barriers effectively block transport of atmospheric pollutants which accumulate along their windward slopes

(Sundström et al., 2012). The concentration of heavy industries and power generation facilities in the NCP are primarily responsible for the observed high AOD concentrations, together with meteorological and geographical conditions. Additionally, lower AOD values appear in southern Anhui and central Shandong relative to the surrounding regions.

The CER spatial distributions (Fig. 3b,e) reveal distinct differences between the two periods. During 2008-2014, larger cloud droplets predominated in the northern sectors, particularly throughout Hebei and western Shandong. Notably, the spatial correspondence between AOD and CER maxima aligns with the anti-Twomey effect, suggesting that the high aerosol loading promoted cloud droplet growth rather than suppression - consistent with findings from Wang et al. (2014) and Liu et al. (2018). The 2015-2022 period shows markedly reduced CER values (typically <10 μm) with enhanced spatial homogeneity.

Similarly, N_d exhibits contrasting spatial patterns between the two periods (Fig. 3c,f). The earlier timeframe shows depressed N_d values in central regions surrounded by elevated concentrations peripherally. This pattern reverses during 2015-2022, with increases of N_d in the central area accompanied by overall reduction of the cloud droplet concentrations in the surrounding regions.

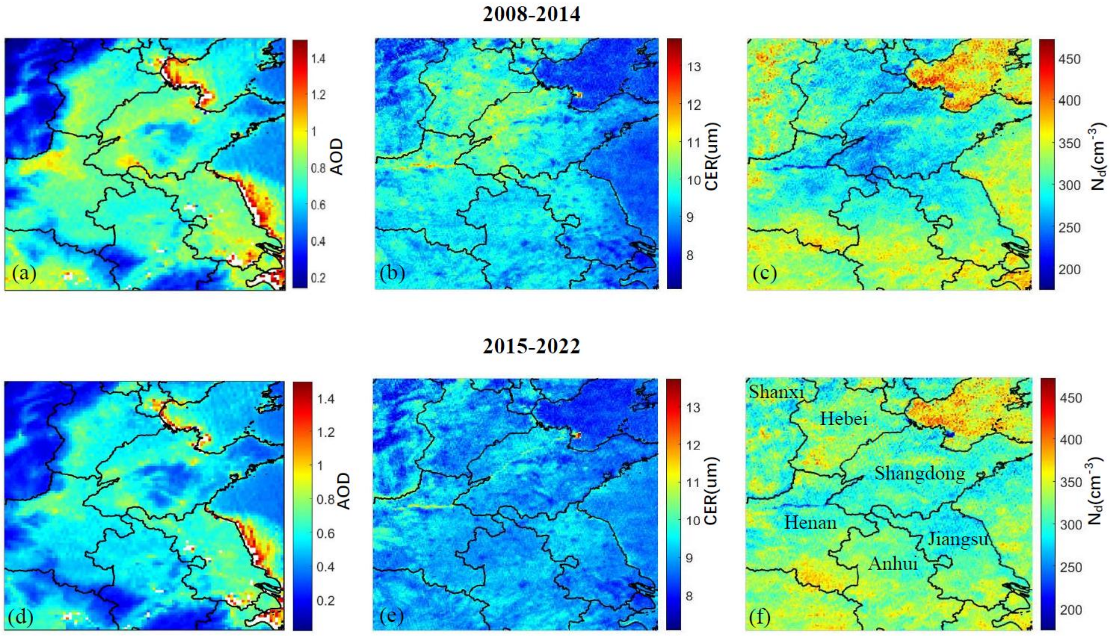

Figure 3. Spatial distributions of AOD (a, d), CER (b, e) and N_d (c, f), averaged over the years 2008-2014 (top row) and 2015-2022 (bottom row) over the study area. The lines are provincial borders and the names of provinces mentioned in the text are indicated in Fig. (f).

3.2 Sensitivity of CER to AOD stratified by LWP

Before analyzing the influence of AOD on CER, the relationship between CER and LWP should be investigated. The values of the LWP were divided into 40 subsets with a width of 5 g/m^2, and then the average value of CER in each subset was calculated and plotted as function of LWP (Figure 4).

The variation of CER with LWP shows three regimes. For LWP smaller than 55 g/m^2 (period 1) or 50 g/m^2 (period 2), CER increased rapidly with the increase of LWP. This first LWP regime is referred to as a rapid growth regime (LWP1). The second LWP regime, referred to as a decreasing regime (LWP2), applies to the LWP range from 55 g/m^2 to 135 g/m^2 (period 1) or 50-100 g/m^2 (period 2) and CER decreased with the increase of LWP. When LWP was greater than 135 g/m^2 (period 1) or 100 g/m^2 (period 2), CER increased with increasing LWP but at a much slower rate than during the first regime; the third LWP regime is therefore referred to as a slow growth regime (LWP3). These results show that CER is very sensitive to the changes in LWP, which is consistent with the study of Liu et al. (2021). Specifically, CER exhibited a three-stage variation with LWP: rapid growth when LWP < 50 g/m^2 (with the fastest change rate), a stable state during 50–150 g/m^2, and slow growth when LWP > 150 g/m^2 (at a rate much lower than the first stage). This highlighted the necessity of fixing LWP conditions to accurately investigate the impact of AOD on CER. To separate the effects of changing LWP on CER from those of changing AOD on CER, relations between CER and AOD were evaluated for constant LWP (McComiskey et al., 2012), for each of the three regimes mentioned above, by using double-logarithmic plots of AOD versus CER. The number of CER observations in the third regime is too small to achieve statistically meaningful results, therefore the sensitivity of CER to AOD was only analyzed for the rapid growth and decreasing regimes.

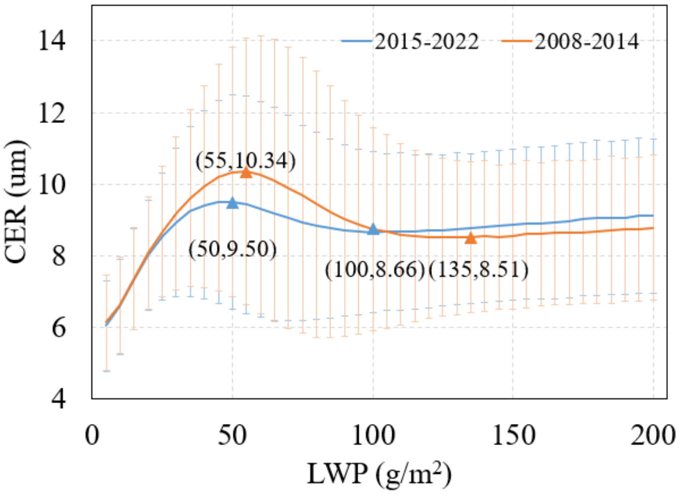

Figure 4. Variation of CER with LWP over the study area. Here all CER data were averaged in LWP bins, from 0 to 200 g/m^2 with a width of 5 g/m^2. The red line is a fit to the data during 2008-2014 and the blue line for the data during 2015-2022. The numbers in parentheses indicate the (LWP, CER) values for the inflection

points between the regimes. The error bars (the vertical lines) denote the standard deviations, indicating the variability of CER around the average at each LWP value.

3.2.1 Rapid CER growth regime

For the first LWP regime, the S_{CER} is negative (as shown in Figure 5). This aligns with the Twomey effect (Twomey, 1977): an increase in aerosols raises the number of CCN, and with constant LWP, less water vapor is available per cloud droplet, reducing CER, increasing cloud albedo, and ultimately cooling the atmosphere. This indicates that, in the rapid growth regime, the interaction between AOD and CER in the target region is in agreement with the Twomey effect. The data in Figure 5a show that during period 1, S_{CER} varies with buffer size and that the variations are different for different study areas. The value of $|S_{CER}|$ is smallest for the largest study area (10°×10°) and decreases with buffer size to a minimum for buffer size of 150 km and then increases. For the smallest study area (4°×4°), the sensitivity exhibits a much stronger negative correlation, with its magnitude decreasing as the buffer size expands, especially for 50 km < buffer size < 100 km. For the 2 intermediate study areas, the sensitivities are initially similar (except for the smallest buffer size) and diverge for buffer size>100 km. The data show that the value of $|S_{CER}|$ overall becomes smaller as study area increases. The decrease of $|S_{CER}|$ with increasing study area is mechanistically tied to scale-dependent aerosol indirect effect theory and meteorological confounding (Quaas et al., 2009; McComiskey & Feingold, 2012). The correlation coefficients R (bottom of Figure 5 a) are similar for all four study areas at small buffer sizes, increase fast with buffer size to a maximum for a buffer size of about 50 km and then decrease and diverge. The largest decrease is observed for the study area of 10°×10°. In this study, the optimal scale for each study area is indicated in Figure 5 with a red solid square. A plot of the optimal scale versus the size of the study area in Figure 6 (curve LWP1-period1) shows that, as the study area size increased from 6°×6° to 10°×10°, the optimal scale decreased from 100 km to 30 km.

As compared with period 1, in period 2 (Figure 5b) the value of the $|S_{CER}|$ also decreases as the buffer size increases. However, the scale sensitivity analysis for period 2 reveals two distinct characteristics different from period 1: (1) the four S_{CER} curves for different study areas are much closer than during period 1; (2) with the exception of the study area of 10°×10°, the values of the $|S_{CER}|$ for the other three study areas are significantly reduced (closer to zero), indicating a corresponding weakening of aci intensity against the background of decreased aerosol concentrations. Particularly noteworthy is that during period 1, the R values for the 10°×10° study area show a sharp declining trend when the buffer size exceeds 60 km, while in period 2 this happens for buffer size larger than 110 km and the R value curves for all study areas significantly expand their high-value ranges. Also for period 2, the R values for the study areas of 10°×10° and 8°×8° are very similar, in contrast to period 1 when only the R values for the study areas of 10°×10° decreases fast. Across different study areas, the optimal scale (Curve LWP1-peirod2) shows a behavior opposite to that during period 1: as the study area size increases from 6°×6° to 10°×10°, the optimal scale increases from 20 km to 80 km. It is noted that for a study area of 4°×4° the optical scale is 50 km in both periods. For the first LWP regime, S_{CER} estimates and correlation coefficients R by period and optimal buffer size across 4°×4° to 10°×10° study areas are given in Appendix A1.

3.2.2 Decreasing CER regime

During the second LWP regime (Figure 7), the AOD and CER is also negatively correlated ($S_{CER}<0$) during both periods, but the values of S_{CER} vary stronger with the size of study area: the curve dispersion increases in the second LWP regime, the values of $|S_{CER}|$ are larger overall, and the relatively concentrated trend in the period 1 shifts to more scattered fluctuations in the period 2. During period 1, for the largest (10°×10°) study area: the value of $|S_{CER}|$ (Figure 7a) decreases with increasing buffer size, nearing zero at ~150 km, briefly turning slightly positive, then slowly falling below zero by 220 km. For the three smaller study areas, the S_{CER} values are all negative and $|S_{CER}|$ overall decreased with increasing buffer size. Through the sensitivity of S_{CER} to buffer size across varying study areas during period 1, the value of $|S_{CER}|$ for a given buffer size becomes smaller with increasing study area size. Additionally, across all study areas, $|S_{CER}|$ initially increases with the increase of the buffer size, then decreases, and gradually stabilizes thereafter. The data in Figure 6 (Curve LWP2-peirod1), show that, the optimal size varies between 30 km and 60 km with no clear dependence on the size of the study area.

Compared with period 1, the value of $|S_{CER}|$ in period 2 (Figure 7b) also decreased overall with increasing buffer size, and at the same buffer size, $|S_{CER}|$ decreased as study area increased. However, the scale sensitivity analysis for period 2 revealed two distinct characteristics: (1) the four curves for different study areas were closer than during period 1; (2) the $|S_{CER}|$ for the study area of 10°×10° was overall larger, while the values of the S_{CER} curves for the study areas of 4°×4° and 6°×6° were significantly reduced and that for the study area of 8°×8° was slightly reduced. The reduction may be attributed to weakened aci resulting from decreased regional aerosol concentrations (Jia et al., 2022; Li et al., 2024; Zhao et al., 2025). The variation of the optimal scale (Curve LWP2-period2) with the size of the study area is similar to that during period 1 in the rapid growth LWP regime: as the study area size increased from 6°×6° to 10°×10°, the optimal scale increased from 60 km to 100 km. For the second LWP regime, S_{CER} estimates and correlation coefficients R between CER and AOD by period and optimal buffer size across 4°×4° to 10°×10° study areas are given in Appendix A1.

Through comparative analysis of S_{CER} data distribution across different LWP regimes under different aerosol conditions (i.e. high AOD and decreasing AOD), we found that the $|S_{CER}|$ in the second LWP regime was significantly larger than that in first LWP regime except for the study area of 10°×10° for buffer size >100 m, where S_{CER} curves corresponding to different study areas showed greater dispersion. This pattern highlights the dominant role of LWP in regulating aci sensitivity, with AOD variations further modulating the magnitude of such differences. Sample sizes of CER and AOD for the first LWP regime across both study periods, all buffer sizes and study areas, are presented in Appendices A3–A6.

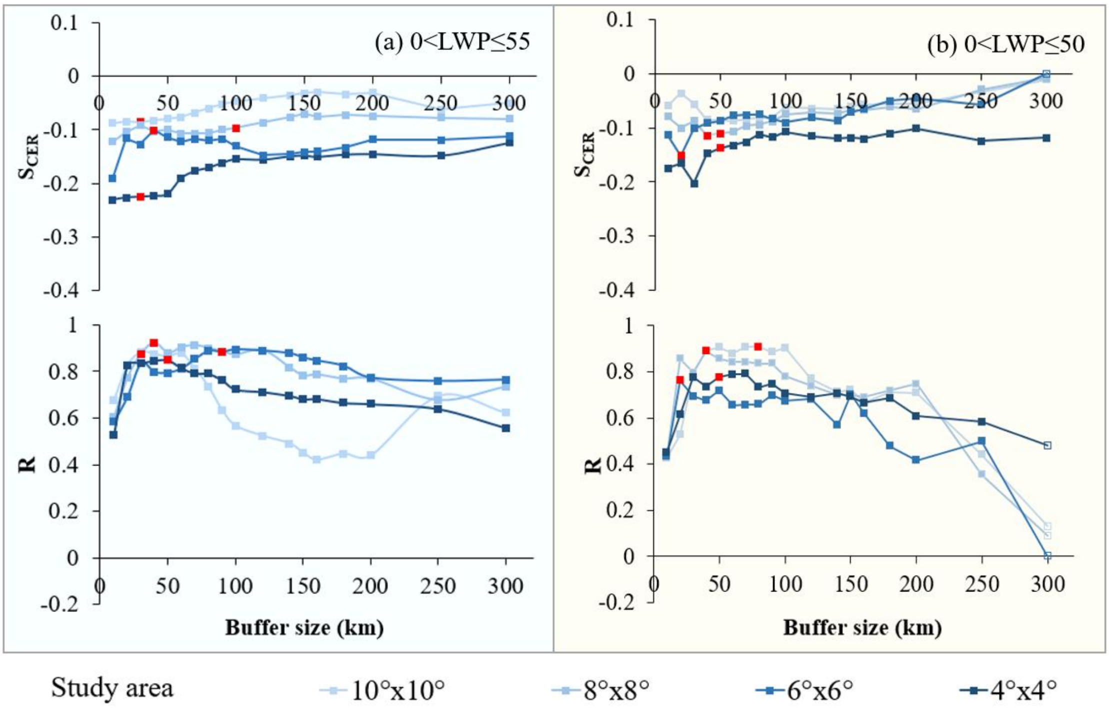

Figure 5. Variation of S_{CER} (top) and correlation coefficient R (bottom) with buffer size for different study areas (see legend at the bottom) for (a) the LWP regime with 0<LWP≤55 g/m^2 over the years 2008-2014 and (b) the LWP regime with 0<LWP≤50 g/m^2 over the years 2015-2022. Filled squares indicate that the results are significant at the 0.01 level and open squares indicate that the results are not statistically significant. Red solid squares indicate the optimal buffer sizes for each study area, as shown in Appendix A1.

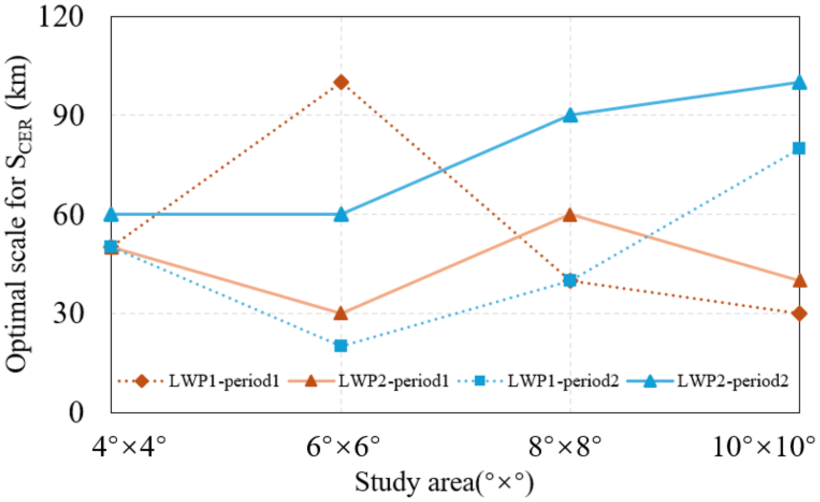

Figure 6. Relationship between optimal scale for S_{CER} and the size of the study area. Here LWP1-period1 and LWP2-period1 indicate the optimal scale in period 2008-2014 for the first LWP regime and that for the second LWP regime, respectively. LWP1-period2 and LWP2-priod2 indicate the optimal scale in period 2015-2022 for the first LWP regime and that for the second LWP regime, respectively.

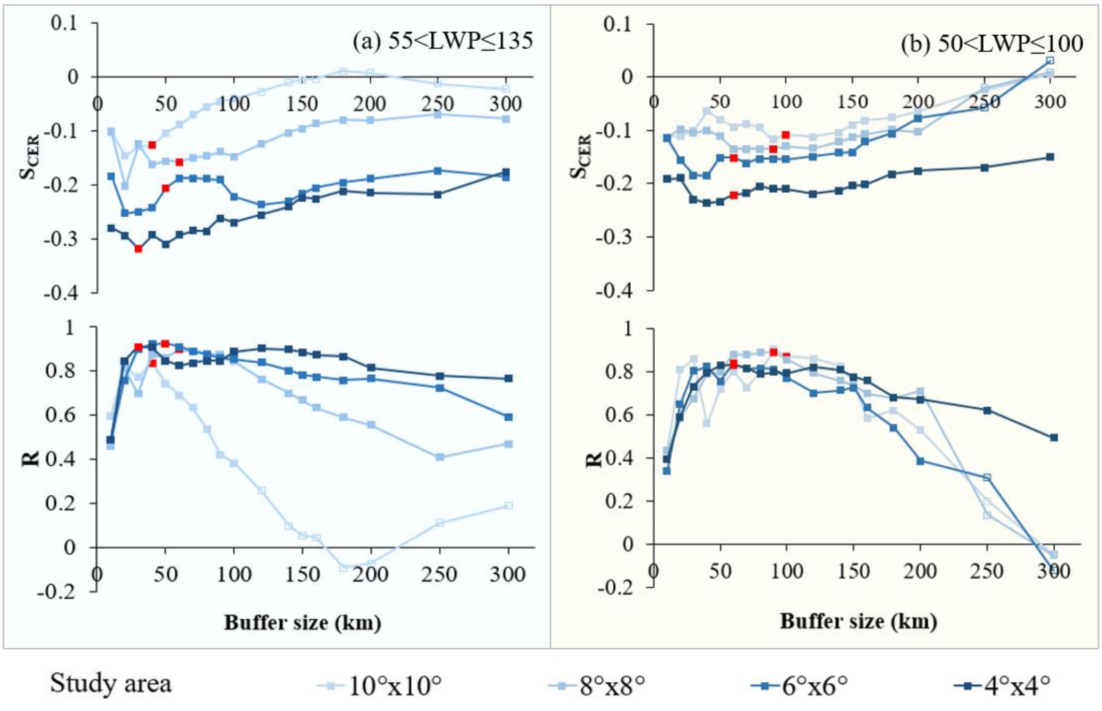

Figure 7. Variation of S_{CER} (top) and correlation coefficient R (bottom) with buffer size for different study areas (see legend at the bottom) for (a) the LWP regime with 55<LWP≤135 g/m^2 over the years 2008-2014 and (b) the LWP regime with 50<LWP≤100 g/m^2 over the years 2015-2022. Filled squares indicates that the results are significant at the 0.01 level and the open squares indicates that the results are not statistically significant. Red solid squares indicate the optimal buffer sizes for each study area, as shown in Appendix A1.

3.3 Sensitivity of N_d to AOD

The sensitivity S_{Nd} is defined as the slope of a linear fit to a log-log plot of S_{Nd} versus AOD (Eq. 2). For each period, we binned the data into AOD intervals of 0.02 and averaged N_d within each bin. Figure 8 shows the variation of S_{Nd} with buffer size for different study areas. In contrast to S_{CER}, S_{Nd} is predominantly positive ($p<0.01$) in both periods and decreases with increasing buffer size. During period 1 (2008–2014, high AOD), S_{Nd} for the 6°×6° study area decreases rapidly to a minimum at buffer sizes of 40-50 km, then increases to a maximum at a buffer size of 120 km. For buffer size ≥ 120 km, the two smallest study areas (4°×4° and 6°×6°) yield similar S_{Nd} values, which are substantially larger than those for the two larger study areas (8°×8° and 10°×10°). During period 2 (2015–2022, decreasing AOD), we can see an initial increase of S_{Nd} for the study area of 6°×6° and 8°×8°, and variation of S_{Nd} for the study area of 10°×10° and 4°×4°. After that, S_{Nd} for the study area of 4°×4° and 6°×6° decreases rapidly to a minimum for a buffer size of 80 km, followed by an increase to a maximum for a buffer size of 140 km. The optimal buffer sizes (maximizing R) are larger for the 8°×8° and 10°×10° study areas than for the 8°×8° and 10°×10° areas (Fig. 9), reflecting different aci characteristics under varying AOD conditions. Estimates of S_{Nd} and R, stratified by optimal buffer size, for study areas ranging from 4°×4° to 10°×10° during the two periods are presented in the Appendix A2.

Expanding the study area inevitably increases spatial heterogeneity in aerosol loading, meteorology, and cloud type, while also introducing larger satellite retrieval uncertainties. This spatial mixing blends clean and polluted air masses, thereby introducing a statistical dilution effect on the estimated S_{Nd}. Therefore, the decrease in S_{Nd} with increasing study area size (Fig. 8) reflects not only a genuine weakening of aerosol-cloud interactions but also the combined effects of meteorological confounding, cloud regime transitions, and retrieval limitations. It is noted that S_{CER} and S_{Nd} exhibit distinct anomalies in large buffer zones, which may be associated with all these factors.

Changes in aerosol chemical composition between the two periods may also modulate S_{Nd}. During 2008–2014, aerosols over eastern China were dominated by sulfate (30%–40% of $PM_{2.5}$ mass; Huang et al., 2014; Zheng et al., 2018). Given the strong hygroscopicity of sulfate-dominated aerosols (Zhang et al., 2012; Liu et al., 2023), their CCN activation efficiency was likely high, providing a favorable physical basis for aci (Lee et al., 2009). In contrast, during 2015–2022, policy interventions (e.g., the Air Pollution Prevention and Control Action Plan; Zheng et al., 2018) drove a structural transition: the sulfate mass fraction dropped sharply to 15%–25% (an absolute reduction of >50%), while less hygroscopic components (nitrate, carbonaceous aerosols, and secondary organic aerosols) increased in relative proportion (Huang et al., 2014; Zheng et al., 2018). As these components generally exhibit weaker hygroscopicity compared with sulfate (Zhang et al., 2012; Liu et al., 2023), this compositional shift may have reduced CCN activation efficiency under the same AOD, thereby weakening the sensitivity of N_d to AOD and altering aci intensity (Lee et al., 2009).

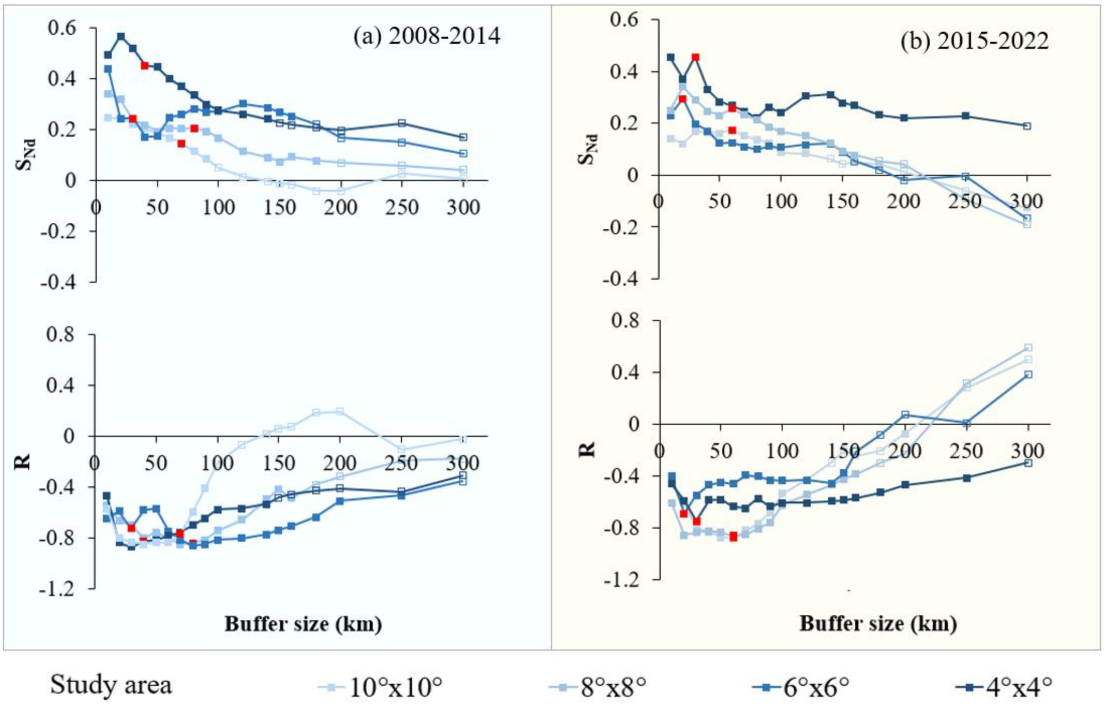

Figure 8. Variation of S_{Nd} (top) and correlation coefficient R (bottom) with buffer size for different study areas (see legend at the bottom) for the LWP regime with $0<LWP\leq200$ g/m^2 over the years 2008-2014 (a) and 2015-2022 (b). Filled squares indicates that the results are significant at the 0.01 level and open squares indicate that the results are not statistically significant. Red solid squares indicate the optimal buffer size for each study area, as shown in Appendix A2.

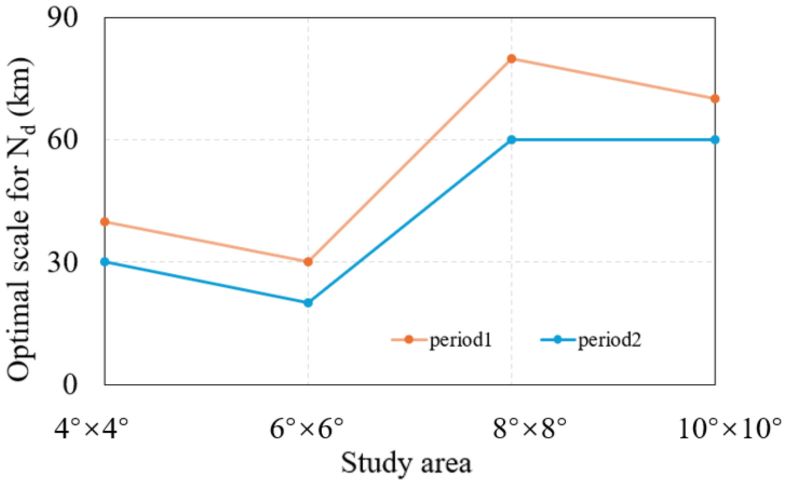

Figure 9. Relationship between optimal scale for N_d and the size of the study area. Here period1 and period2 indicate the optimal scale in period 2008-2014 and the optimal scale in period 2015-2022, respectively.

4 Discussion

4.1 The importance of liquid water path constraint

LWP is a critical parameter governing cloud radiative properties (Murray-Watson et al., 2022). The quantification of albedo effects strongly depends on the spatial scale and the LWP. Neglecting LWP constraints in aci studies can weaken microphysical signals, leading to underestimation of radiative forcing (McComiskey et al., 2012). To address this, we first systematically investigated the dynamic relationship between CER and LWP before analyzing CER sensitivity to AOD. The results demonstrate pronounced CER sensitivity to LWP variations, which can be categorized into three distinct regimes (Figure 4):

In the first LWP regime, CER increases rapidly with LWP, i.e. the evolution of CER is predominantly driven by changes in LWP. This dominance may lead to overestimation of the influence of the AOD on CER (Liu et al., 2021).

In the second LWP regime, CER decreases with increasing LWP. In this regime, the regulatory effect of LWP on CER weakens significantly, and CER variations become increasingly governed by aerosol-related processes, indicating the growing dominance of aerosol indirect effects.

The third regime contains an insufficient number of CER observations to yield statistically significant results, which excludes the analysis of the sensitivity of CER to AOD.

Comparative analysis of scale-conditioned S_{CER} across LWP regimes in periods 1 and 2 revealed markedly enhanced sensitivity of S_{CER} to AOD in the second LWP regime. A trade-off exists between AOD and LWP under conditions of insufficient water vapor. This trade-off leads to smaller CER values. As suggested by Costantino et al. (2013), the LWP response to aerosol invigoration is influenced by two competing mechanisms: a drying effect caused by enhanced entrainment of dry air at cloud top (dominant in optically thin clouds) and a moistening effect from precipitation suppression (dominant in optically thick clouds). For larger LWP, the supply of cloud water is sufficient. The increase in aerosol number concentrations significantly affects the distribution of cloud droplet number concentrations and sizes. This further enhances the sensitivity of CER to AOD. For small aerosol concentrations, the values of $|S_{CER}|$ (Figure 5b, 7b) decreased overall with expanding buffer size within the same study area. For fixed buffer size, $|S_{CER}|$ decreased as the study area increased. The ranges of $|S_{CER}|$ values across different study areas showed a convergent pattern. These values typically remained small and close to zero. During the high AOD period (2008–2014), anthropogenic emissions and dust transport provided abundant CCN. This laid the material foundation for strong aci. It enhanced the synergistic effect of “sufficient liquid water + abundant CCN” in the second LWP regime. This synergistic effect amplified the difference in S_{CER} between the two LWP regimes. In the period of decreasing AOD (2015–2022), CCN concentration decreased following the implementation of clean air policies (de Leeuw et al., 2021; 2023). This reduction weakened the direct impact of aerosols on CER. However, the LWP-driven microphysical differences persisted. Thus, S_{CER} in the second regime remained significantly smaller than that in the first regime, albeit with a smaller difference. Additionally, the complexity of aerosol types during the high AOD period (e.g., mixing of anthropogenic pollutants and natural dust) may have adjusted the value of S_{CER}. However, it did not alter the dominant role of LWP. This aligns with the theory that “aerosol indirect effects are jointly regulated by concentration and type” (Liu et al., 2017).

The larger S_{CER} observed at larger spatial scales (Figures 5 and 7) may be attributed to meteorological confounding effects. In addition, clouds with larger LWP are usually associated with strong updrafts (such as convective clouds), and stronger turbulence and vertical transport will bring more aerosols into the clouds, increasing CCN concentration and a decrease in particle size, making them more sensitive to changes in AOD (Jones et al., 2009; Han et al., 2022; Fan et al., 2025). Therefore, this phenomenon is the result of the combined action of cloud microphysical processes (CCN activation, cloud droplet competition growth) and dynamic processes (updrafts, turbulent mixing). If the characteristics of aerosols (such as composition) change in the second LWP regime, this sensitivity may be further amplified. Consequently, the LWP-stratified S_{CER} quantification framework enables precise characterization of scale-dependent aci, providing robust physical insights for climate effect assessments and effectively reducing uncertainties in future climate projections.

The central hypothesis of this study—that LWP is relatively consistent between the two periods (2008–2014 and 2015–2022), supporting valid comparisons of the spatial sensitivity of AOD-CER relationships—is well-supported by the following analysis. The differences in the mean, median, 25th, and 50th percentiles of LWP between the two periods are all less than 5%, indicating a stable overall water vapor supply level. The spatial patterns of high-LWP regions (e.g., southeastern areas) and low-LWP regions (e.g., the mountainous areas in northern Shanxi) remained stable across the two periods (see Appendix B1), demonstrating that LWP spatial distribution characteristics are highly consistent. The sample proportions of LWP in the rapid growth regime are 59.30% (period 1: 0–55 g/m²) and 55.36% (period 2: 0–50 g/m²), while those in the decreasing regime are 29.64% (period 1: 55–135 g/m²) and 24.59% (period 2: 50–100 g/m²), suggesting that there is no systematic temporal shift in the LWP distribution. Meanwhile, short-term fluctuations are smoothed by multi-year averaging and large-sample statistics, resulting in a weak indirect impact of aerosols on LWP (LWP only increased by 5.6%, much smaller than the 24% decrease in AOD). Additionally, LWP-stratified analysis (i.e., binning LWP into 5 $g\ m^{-2}$ intervals) further isolates interference. The validation of the core hypothesis provides a reliable premise for accurately quantifying the impact of aerosol concentration changes on the sensitivity of cloud parameters and their spatial scale dependence.

4.2 Scale dependence of cloud parameters sensitivities to aerosol variations

Extensive studies have demonstrated a significant spatial scale dependence of aerosol indirect effects (McComiskey et al., 2012; Possner et al., 2016; Glotfelty et al., 2020; Ekman et al., 2023). Failure to explicitly define the scale-dependent behavior of aerosol indirect effects may introduce systematic biases and inconsistencies in subsequent process analyses. Based on satellite observations, this study confirms statistically significant negative correlations between CER and AOD, as well as positive correlations between N_d and AOD during periods with different aerosol concentrations, aligning with classical aci theory (Quaas et al., 2009). Analysis of scale-conditioned S_{CER} and S_{Nd} reveals that for fixed buffer size, an increase in the size of the study area leads to a systematic reduction in S_{CER} (less negative) and S_{Nd}, corroborating the nonlinear attenuation of aerosol signals with spatial domain expansion (Quaas et al., 2009). The results from this study suggest that AOD-cloud property correlations in large study areas are susceptible to meteorological confounding effects (Quaas et al., 2010; Boucher and Quaas, 2012; Gryspeerdt et al., 2014; Liu et al., 2024). Theoretically, aerosol regulation of cloud microphysics is strongly local: smaller domains (e.g., 4°×4°) feature homogeneous meteorological conditions (humidity, updrafts), preserving undiluted aci signals and yielding larger $|S_{CER}|$ (pronounced Twomey effect). In contrast, expanded domains (e.g., 10°×10°) encompass heterogeneous meteorological conditions (circulation differences, boundary layer variability) that independently modulate cloud droplet growth. For example, strong updrafts enhance liquid water supply, offsetting aerosol-induced radius reduction (Altaratz et al., 2014), weakening aerosol-CER correlations and reducing $|S_{CER}|$. Consistent with Grandey

& Stier (2010), large-scale domains introduce “dilution bias” via non-target meteorological variability. This scale-dependent confounding mechanism elucidates uncertainties in aerosol indirect effect assessments at regional scales.

Multi-scale spatial analysis identifies different optimal buffer sizes for S_{CER} and S_{Nd} in different periods. These findings align closely with satellite-based aerosol indirect effect studies (Wang et al., 2015; Liu et al., 2017), providing critical scale benchmarks for satellite product validation. Wang et al. (2015) reported an inverse "Twomey" effect between aerosols and CER in eastern China by analyzing aerosol and CER within a 50 km buffer zone around CALIOP samples. Similarly, Liu et al. (2017) systematically examined the response mechanisms of warm cloud macro- and microphysical parameters to increasing AOD in the Yangtze River Delta region, also using CALIOP samples within a 50 km buffer zone. The present study further shows that, as aerosol concentrations decrease, S_{CER} values across different study areas with the same buffer size exhibit convergence characteristics, with generally smaller S_{CER} (closer to zero). This indicates a significant weakening of aci intensity and reduced spatial extent dependency in low aerosol loading conditions. This phenomenon is consistent with the simulated behavior of aerosol-limited cloud regimes, where aci are quantitatively modulated by moisture availability and lose their sensitivity to large-scale dynamical stability, leading to a weaker and more homogeneous effect (Zhao et al., 2025).

By systematically quantifying the scale-response characteristics of aerosol indirect effects, this work not only elucidates the dynamic scale behavior of aci, but also, more critically, establishes criteria for determining optimal buffer size in regional aerosol indirect effect studies. These results provide quantitative observational constraints for refining scale-dependent parameterization modules in climate models, particularly for representing the modulation of ACI by spatial scale and LWP, thereby improving model predictive reliability.

4.3 Contrasting sensitivity patterns of cloud parameters in response to AOD

A comprehensive comparison of the sensitivity S_{CER} and S_{Nd} reveals that the responses of CER and N_d to AOD exhibit distinct yet inherently interconnected characteristics. These characteristics are jointly modulated by spatial scale and LWP regimes (Figs. 5, 7, 8; Appendices A1–A2), which profoundly reflect the core microphysical mechanisms of aci. Details are elaborated as follows:

4.3.1 Core differences in response modes between S_{CER} and N_d to AOD

S_{CER} is consistently negative across both periods and all LWP regimes ($-0.33<S_{CER}<0$) (Figs. 5, 7; Appendix A1), indicating that an increase in AOD leads to a decrease in CER. This aligns with the core principle of the Twomey effect (Twomey, 1977; Feingold et al., 2001). The values of $|S_{CER}|$ are larger in the second LWP regime than in the first regime, reflecting stronger aerosol modulation of cloud microphysical properties when liquid water is abundant (McComiskey & Feingold, 2012). In contrast, S_{Nd} maintains a significant positive correlation with AOD across all scenarios ($0<S_{Nd}<1$) (Fig. 8; Appendix A2), confirming that higher AOD directly promotes CCN activation and thereby increases cloud droplet number concentration (Andreae, 2009).

4.3.2 Synergistic modulation of AOD and spatial scale

Using the LWP interval corresponding to S_{Nd} ($0 < \text{LWP} \leq 200$ g/m²) as a benchmark, comparisons between the two periods (incorporating average values of S_{CER} across two LWP regimes) reveal distinct characteristics:

For the small-scale study area (4°×4°): In period 1, the average $|S_{CER}|$ across two LWP regimes is 0.271 (0.2232 for the 0–55 g/m² LWP regime, 0.3189 for the 55–135 g/m² LWP regime) and S_{Nd}=0.4496, both significantly higher than those in period 2 (average $|S_{CER}|$=0.154, with 0.0863 for the 0–50 g/m² LWP regime and 0.2212 for the 50–100 g/m² LWP regime; S_{Nd}=0.2903). The negative correlation between AOD and CER is more significant in period 1, as sufficient CCN in small-scale areas amplifies both cloud droplet number increase and size reduction, enhancing the Twomey effect.

For the medium-to-large scale study areas (6°×6°, 8°×8°, 10°×10°): In period 1, the average $|S_{CER}|$ across the two LWP regimes is 0.1683 (0.1305 for 0–55 g/m², 0.2061 for 55–135 g/m²), 0.13065 (0.1026 for 0–55 g/m², 0.1587 for 55–135 g/m²), and 0.1067 (0.0858 for 0–55 g/m², 0.0885 for 55–135 g/m²), respectively, all higher than the corresponding values in period 2 (0.1516, 0.1246, 0.0985). However, S_{Nd} in period 1 (0.2430, 0.2050, 0.1430) is lower than that in period 2 (0.2960, 0.2680, 0.1740), with no significant difference in the negative correlation between AOD and CER between the two periods.

This characteristic indicates that meteorological confounding effects are enhanced at larger scales, weakening the regulation of S_{Nd} by aerosols, while at small scales the aci is directly driven by AOD levels.

4.4 Limitations and future perspectives

This study has three significant limitations. Firstly, similar to most previous studies (Wang et al., 2015; Liu et al., 2021), this study only utilized MODIS data with a resolution of 10 km to explore scale effects, ignoring finer or coarser resolution data. Therefore, using a 10 km buffer size as the minimum observation unit, this limitation makes the indirect effects of aerosols on smaller scales still unknown, which may lead to inaccurate evaluation of aerosol indirect effects. Therefore, future research can improve the sensitivity of aerosol indirect effects to scale changes by using observation data with higher accuracy or model simulations. Secondly, the current research focuses on the influence of buffer size and study areas, the potential impact of spatial aggregation methods (especially zoning directionality) on the quantitative results of aerosol indirect effects has not been systematically evaluated. Future research should further investigate the sensitivity of aerosol indirect effects to zoning direction. Moreover, the current study employs a uniform buffer size for both aerosol and cloud parameters, failing to account for potential interaction effects arising from discrepancies of buffer size between them. Therefore, clarifying scale dependence will avoid directly extrapolating local observation results to a larger study area when downscaling climate models or formulating regional environmental policies.

5 Conclusions

Based on MODIS and CALIOP satellite observations of aerosol and cloud parameters over land in eastern China, a comparative analysis was conducted of the sensitivity of cloud microphysical parameters (CER and N_d) to variations in AOD during two characteristic periods: 2008–2014 (period 1, high AOD) and 2015–2022 (period 2, decreasing AOD). Through systematic analysis of the relationship between CER and LWP and their response mechanisms to AOD across these two periods, the following key conclusions were drawn:

Firstly, CER exhibited three distinct regimes with varying LWP. During the rapid growth regime (LWP < 55/50 g/m²), CER showed significant negative sensitivity to AOD (S_{CER}), consistent with the Twomey effect; during the decreasing regime (LWP = 55-135/50-100 g/m²), S_{CER} remained negative but with enhanced sensitivity; and during the slow growth regime (LWP > 135/100 g/m²), the rate of CER change significantly decreased. These findings confirmed that LWP is a crucial, regulatory factor influencing the CER response to AOD.

Secondly, scale dependence analysis led to the conclusion that characteristics in aci are significantly scale-dependent, with systematic variations of both S_{CER} and S_{Nd} with changes in buffer size and study area. The results of the study show that S_{CER} systematically increased as buffer size increased and became negligible for buffer sizes larger than 150-200 km, while the optimal buffer sizes varied substantially with the size of the study area in the range from 6°×6° to 10°×10°: increased as study area increased during period 2, but decreased in period 1 for regime 2. Particularly noteworthy is the enhanced consistency of S_{CER} across different study areas and the significant increase in S_{CER} during period 2, reflecting weaker aci due to declining regional aerosol concentrations.

Finally, the sensitivity of N_d to AOD (S_{Nd}) exhibited distinct characteristics compared to S_{CER}: S_{Nd} showed a significant positive correlation ($p < 0.01$) and demonstrated nonlinear attenuation with increasing buffer size and study area. The optimal buffer size for S_{Nd} was smaller during period 2 than during period 1 and increased with the study area size, being substantially larger for study areas of 8°×8° and 10°×10° than for study areas of 4°×4° and 6°×6° areas.

These observed patterns correspond to the fundamental microphysical pathway of aci, whereby increased aerosol loading enhances N_d and reduces CER under constant LWP conditions. The results emphasize that accurate quantification of ACI must explicitly consider both the phase-dependent characteristics of LWP and spatial scale effects when assessing aerosol indirect effects.

These findings deepen our understanding of aerosol indirect effects and provide quantitative observational constraints for improving aerosol–cloud parameterization in climate models. Our results highlight that ACI parameterization should explicitly incorporate LWP regime-dependent behavior and spatial scale-dependent interaction strengths to improve realistic representation.

Appendix

A1. Estimates of S_{CER}, computed using Eq. (1), and correlation coefficients R between CER and AOD, stratified by LWP, and optimal buffer size (see text), for study areas varying from 4°×4° to 10°×10°, during the periods 2008-2014 and 2015-2022. Statistically significant data points are indicated with * (p value < 0.01).

Years	LWP（g/m^2）	Study area	Optimal scale (km)	S_{CER}	R
2008-2014	0-55	10°×10°	30	-0.0858	0.8828*
		8°×8°	40	-0.1026	0.9220*
		6°×6°	100	-0.1305	0.8939*
		4°×4°	50	-0.2232	0.8459*
	55-135	10°×10°	40	-0.1275	0.8377*
		8°×8°	60	-0.1587	0.8978*
		6°×6°	30	-0.2061	0.9245*
		4°×4°	50	-0.3189	0.9096*
2015-2022	0-50	10°×10°	80	-0.0885	0.9082*
		8°×8°	40	-0.1138	0.8886*
		6°×6°	20	-0.1517	0.7618*
		4°×4°	50	-0.0863	0.6403*
	50-100	10°×10°	100	-0.1084	0.8717*
		8°×8°	90	-0.1354	0.8910*
		6°×6°	60	-0.1514	0.8384*
		4°×4°	60	-0.2212	0.8318*

A2. Estimates of S_{Nd}, computed using Eq. (2), and correlation coefficients R between N_d and AOD, stratified by optimal buffer size (see text) for study areas varying from 4°×4° to 10°×10°, during the periods 2008-2014 and 2015-2022. Statistically significant data points are indicated with * (p value < 0.01).

Years	Study area	Optimal scale (km)	S_{Nd}	R
2008-2014	10°×10°	70	0.1434	-0.8507*
	8°×8°	80	0.2045	-0.8646*
	6°×6°	30	0.2430	-0.8741*
	4°×4°	40	0.4496	-0.8523*
2015-2022	10°×10°	60	0.1742	-0.8788*
	8°×8°	60	0.2682	-0.8638*
	6°×6°	20	0.2964	-0.6900*
	4°×4°	30	0.2903	-0.7478*

A3. Sample sizes of cloud droplet effective radius (CER) and aerosol optical depth (AOD) across different buffer sizes, study areas (LWP regime 1, 2008–2014).

Buffer sizes	Sample sizes of CER in LWP regime 1				Sample sizes of AOD in LWP regime 1			
	10°×10°	8°×8°	6°×6°	4°×4°	10°×10°	8°×8°	6°×6°	4°×4°
10	25054	16133	8551	3879	47846	32406	18711	8808
20	41667	26507	14077	6376	64878	42949	24462	11377
30	54960	34885	18421	8346	76569	50055	28274	13047
40	66170	42147	22136	9966	86291	56006	31523	14482
50	76207	48769	25738	11593	94726	61227	34272	15664
60	85194	54539	28946	12979	102262	65860	36741	16695
70	93413	59681	31788	14192	108792	69756	38749	17519
80	100728	64370	34330	15317	114357	73103	40498	18246
90	107291	68535	36552	16270	119187	76077	42016	18893
100	113457	72525	38761	17155	123607	78839	43496	19469
120	124793	79882	42945	18964	131449	83807	46217	20534
140	134597	86324	46525	20462	138140	88001	48518	21557
150	138760	89086	48145	21141	141012	89985	49570	21991
160	142693	91808	49602	21734	143725	91767	50570	22436
180	150015	96789	52326	22860	148480	94870	52385	23155
200	156655	101246	54894	23983	153084	97946	53963	23921
250	169423	109475	59449	26008	162530	104346	56987	25388
300	178015	115051	62656	27442	170117	109006	59332	26453

A4. Sample sizes of cloud droplet effective radius (CER) and aerosol optical depth (AOD) across different buffer sizes, study areas (LWP regime 2, 2008–2014).

Buffer sizes	Sample sizes of CER in LWP regime 2				Sample sizes of AOD in LWP regime 2			
	10°×10°	8°×8°	6°×6°	4°×4°	10°×10°	8°×8°	6°×6°	4°×4°
10	22338	14357	7737	3715	47846	32406	18711	8808
20	35406	22471	11964	5697	64878	42949	24462	11377
30	45473	28805	15162	7187	76569	50055	28274	13047
40	54074	34078	17839	8368	86291	56006	31523	14482
50	61579	38732	20290	9444	94726	61227	34272	15664
60	68173	43017	22553	10424	102262	65860	36741	16695
70	74272	46909	24584	11230	108792	69756	38749	17519
80	79999	50507	26412	11950	114357	73103	40498	18246
90	85339	53806	28177	12654	119187	76077	42016	18893
100	90440	56944	29812	13329	123607	78839	43496	19469
120	99758	62598	32673	14486	131449	83807	46217	20534
140	108723	68273	35600	15795	138140	88001	48518	21557
150	112740	70969	36864	16426	141012	89985	49570	21991
160	116558	73463	38046	16974	143725	91767	50570	22436
180	123653	78031	40203	17917	148480	94870	52385	23155
200	129864	81813	42186	18674	153084	97946	53963	23921
250	142429	89112	46079	20120	162530	104346	56987	25388
300	152460	95213	49452	21369	170117	109006	59332	26453

A5. Sample sizes of cloud droplet effective radius (CER) and aerosol optical depth (AOD) across different buffer sizes, study areas (LWP regime 1, 2015–2022).

Buffer sizes	Sample sizes of CER in LWP regime 1				Sample sizes of AOD in LWP regime 1			
	10°×10°	8°×8°	6°×6°	4°×4°	10°×10°	8°×8°	6°×6°	4°×4°
10	25054	16133	8551	3879	47846	32406	18711	8808
20	41667	26507	14077	6376	64878	42949	24462	11377
30	54960	34885	18421	8346	76569	50055	28274	13047
40	66170	42147	22136	9966	86291	56006	31523	14482
50	76207	48769	25738	11593	94726	61227	34272	15664
60	85194	54539	28946	12979	102262	65860	36741	16695
70	93413	59681	31788	14192	108792	69756	38749	17519
80	100728	64370	34330	15317	114357	73103	40498	18246
90	107291	68535	36552	16270	119187	76077	42016	18893
100	113457	72525	38761	17155	123607	78839	43496	19469
120	124793	79882	42945	18964	131449	83807	46217	20534
140	134597	86324	46525	20462	138140	88001	48518	21557
150	138760	89086	48145	21141	141012	89985	49570	21991
160	142693	91808	49602	21734	143725	91767	50570	22436
180	150015	96789	52326	22860	148480	94870	52385	23155
200	156655	101246	54894	23983	153084	97946	53963	23921
250	169423	109475	59449	26008	162530	104346	56987	25388

A6. Sample sizes of cloud droplet effective radius (CER) and aerosol optical depth (AOD) across different buffer size, study areas (LWP regime 2, 2015–2022).

Buffer sizes	Sample sizes of CER in LWP regime 2				Sample sizes of AOD in LWP regime 2			
	10°×10°	8°×8°	6°×6°	4°×4°	10°×10°	8°×8°	6°×6°	4°×4°
10	6548	6548	5449	2803	12892	12892	12892	5961
20	24886	16258	8833	4421	46067	30536	17623	8079
30	32260	20786	11214	5490	55767	36685	20780	9408
40	38784	24739	13284	6440	63457	41493	23310	10474
50	44831	28399	15176	7183	70030	45443	25423	11419
60	50181	31609	16909	7816	75667	48900	27138	12122
70	54865	34476	18456	8415	80872	51807	28559	12723
80	58946	37042	19776	8901	85308	54361	29846	13245
90	62835	39437	21006	9359	89202	56659	31024	13706
100	66623	41757	22165	9796	92939	58931	32143	14126
120	73427	46010	24248	10605	99298	62674	34081	14927
140	79486	49854	26210	11312	104540	65994	36013	15617
150	82336	51650	26988	11633	107089	67545	36876	15939
160	85055	53440	27893	11942	109626	69104	37718	16261
180	89669	56388	29401	12520	114187	72088	39380	16889
200	93898	58986	30700	13034	117969	74508	40596	17401
250	102933	64417	33649	14040	125590	79489	43005	18271
300	109964	68913	35755	14701	132000	83404	45012	18913

A7. Sample sizes of cloud droplet number concentration (N_d) and aerosol optical depth (AOD) across different buffer sizes and study areas during 2008-2014.

Buffer sizes	Sample sizes of N_d				Sample sizes of AOD			
	10°×10°	8°×8°	6°×6°	4°×4°	10°×10°	8°×8°	6°×6°	4°×4°
10	47846	32406	18711	8808	50686	32611	17320	8053
20	64878	42949	24462	11377	70102	45066	23944	11084
30	76569	50055	28274	13047	84442	54334	28822	13435
40	86291	56006	31523	14482	96186	62056	32857	15309
50	94726	61227	34272	15664	106166	68620	36473	16906
60	102262	65860	36741	16695	114950	74328	39638	18292
70	108792	69756	38749	17519	122840	79508	42510	19478
80	114357	73103	40498	18246	129763	84048	45038	20599
90	119187	76077	42016	18893	135810	87931	47225	21548
100	123607	78839	43496	19469	141407	91543	49256	22436
120	131449	83807	46217	20534	151353	98040	53031	24145
140	138140	88001	48518	21557	159758	103516	56167	25517
150	141012	89985	49570	21991	163180	105820	57561	26100
160	143725	91767	50570	22436	166373	108000	58769	26661
180	148480	94870	52385	23155	172007	111773	60981	27665
200	153084	97946	53963	23921	176658	114922	62862	28696
250	162530	104346	56987	25388	185393	120627	66331	30409
300	170117	109006	59332	26453	191138	124592	68823	31481

A8. Sample sizes of cloud droplet number concentration (N_d) and aerosol optical depth (AOD) across different buffer sizes and study areas during 2015-2022.

Buffer sizes	Sample sizes of N_d				Sample sizes of AOD			
	10°×10°	8°×8°	6°×6°	4°×4°	10°×10°	8°×8°	6°×6°	4°×4°
10	37182	23994	13048	6149	31621	21503	12892	5961
20	51313	32990	17755	8252	46067	30536	17623	8079
30	61921	39800	21327	9788	55767	36685	20780	9408
40	70663	45351	24213	11063	63457	41493	23310	10474
50	78059	50080	26808	12118	70030	45443	25423	11419
60	84354	53975	28967	13015	75667	48900	27138	12122
70	89675	57448	30881	13832	80872	51807	28559	12723
80	94620	60671	32636	14556	85308	54361	29846	13245
90	99042	63497	34138	15155	89202	56659	31024	13706
100	102936	65993	35444	15703	92939	58931	32143	14126
120	110590	70884	38002	16787	99298	62674	34081	14927
140	116487	74472	40007	17549	104540	65994	36013	15617
150	119140	76230	41049	17958	107089	67545	36876	15939
160	121506	77846	41958	18265	109626	69104	37718	16261
180	125788	80845	43582	18935	114187	72088	39380	16889
200	129613	83370	44887	19538	117969	74508	40596	17401
250	136752	87967	47756	20784	125590	79489	43005	18271
300	141896	91273	49807	21431	132000	83404	45012	18913

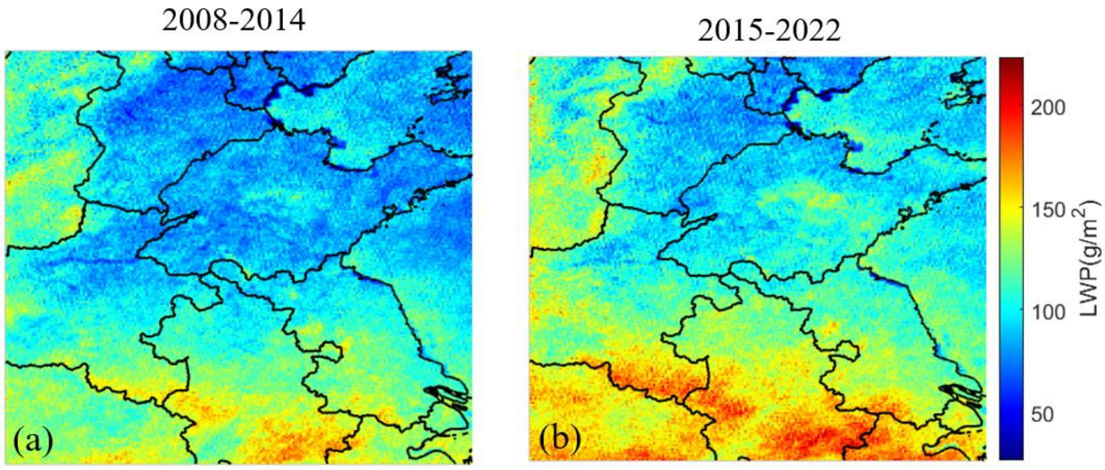

B1. Spatial distributions of LWP averaged over the years 2008-2014 (a) and 2015-2022 (b) over the study area. The lines are provincial borders and the names of provinces mentioned in the text are indicated in Fig. 3(f).

Data availability

All data used in this study are publicly available. The satellite data from the MODIS instrument used in this study were obtained from https://ladsweb.nascom.nasa.gov/search/ (last access: 02 July 2025). The satellite data from CALIOP were obtained from https://subset.larc.nasa.gov/calipso/login.php (last access: 02 July 2025).

Author contributions

YL, LT and GL designed the research. YL and LT led the analyses. YL and GL wrote the manuscript with major input from JH, and further input from all other authors. All authors contributed to interpreting the results and to the finalization and revision of the manuscript.

Competing interests

The authors declare that they have no conflict of interest.

Acknowledgements

The authors greatly appreciate NASA CloudSat Data Processing Center that provided the data used in this study. This work was supported by the National Natural Science Foundation of China (Grant No. 42001290), the Natural Natural Science Foundation of China (Grant No. 42271299), the Natural Science

Foundation Project of Xiamen (Grant No. 3502Z202472037) and the Chinese Academy of Sciences President's International Fellowship Initiative, Grant No. 2025PVA0014_Y1.

References

Albrecht, B. A.: Aerosols, cloud microphysics, and fractional cloudiness, Science, 245, 1227-1230, 1989.

Bellouin, N., Quaas, J., Gryspeerdt, E., Kinne, S., Stier, P., Watson-Parris, D., et al.: Bounding global aerosol radiative forcing of climate change. Reviews of Geophysics, 58, e2019RG000660. https://doi.org/10. 1029/2019RG000660, 2020.

Altaratz, O., Koren, I., Remer, L.A., Hirsch, E.: Review: Cloud invigoration by aerosols—Coupling between microphysics and dynamics. Atmospheric Research, 140-141, 38-60, 2014.

Andreae, M. O.: Correlation between cloud condensation nuclei concentration and aerosol optical thickness in remote and polluted regions, Atmos. Chem. Phys., 9, 543-556, https://doi.org/10.5194/acp-9-543-2009, 2009.

Baum, B. A., et al.: MODIS cloud-top property refinement for Collection 6, J. Appl. Meteorol. Climatol., 51(6), 1145-1163, 2012.

Bender, F.A.M., Frey, L., McCoy, D.T., Grosvenor, D.P., Mohrmann, J.K.: Assessment of aerosol–cloud–radiation correlations in satellite observations, climate models and reanalysis. Climate Dynamics, 52, 4371-4392, 2019.

Boucher, O., Quaas, J.: Water vapour affects both rain and aerosol optical depth. Nature Geoscience, 6(1), 4-5. https://doi.org/10.1038/ngeo1692, 2012.

Bréon, F. M., Tanré, D., Generoso, S.: Aerosol effect on cloud droplet size monitored from satellite, Science, 295(5556):834-8. doi: 10.1126/science.1066434, 2002.

Bulgin, C. E., Palmer, P.I., Thomas, G.E., Arnold, C.P.G., Campmany, E., Carboni, E., Grainger, R. G., Poulsen, C., Siddans, R., Lawrence, B.N.: Regional and seasonal variations of the Twomey indirect effect as observed by the ATSR-2 satellite instrument, Geophysical Research Letters, 35, 2, 2008.

Cai, H., Yang, Y., Chen, Q.: Distribution Characteristics of Cloud Types and Cloud Phases over China and Their Relationship with Cloud Temperature, Remote Sensing, 14(21), 2022. https://doi.org/10.3390/rs14215601

Chen, G., W.-C.Wang, and J.-P. Chen, 2015: Aerosol–stratocumulus–radiation interactions over southeast Pacific. J. Atmos. Sci., 72, 2612–2621, https://doi.org/10.1175/JAS-D-14-0319.1.

Chen, Y.-C., Christensen, M. W., Stephens, G. L., and Seinfeld, J. H.: Satellite-based estimate of global aerosol-cloud radiative forcing by marine warm clouds, Nat. Geosci., 7, 643–646, https://doi.org/10.1038/ngeo2214, 2014.

Christensen, M. W., Chen, Y.-C., and Stephens, G. L.: Aerosol indirect effect dictated by liquid clouds, J. Geophys. Res., 121, 14636-14650, https://doi.org/10.1002/2016JD025245, 2016.

Costantino, L. and Bréon, F. M.: Analysis of aerosol-cloud interaction from multi-sensor satellite observations. Geophys. Res. Lett., 37, L11801, doi:10.1029/2009GL041828, 2010.

Costantino, L. and Bréon, F. M.: Aerosol indirect effect on warm clouds over South-East Atlantic, from co-located MODIS and CALIPSO observations, Atmos. Chem. Phys., 13: 69-88, 2013.

Dagan, G., Yeheskel, N., Williams, A. I. L.: Radiative forcing from aerosol–cloud interactions enhanced by large-scale circulation adjustments, Nature geoscience, 16, 1092-1098, 2023.

de Leeuw, G., R. van der A, J. Bai, Y. Xue, C. Varotsos, Z. Li, C. Fan, X. Chen, I. Christodoulakis, J. Ding, X. Hou, G. Kouremadas, D. Li, J. Wang, M. Zara, K. Zhang, Y. Zhang.: Air Quality over China. Remote Sens. 2021, 13, 3542. https://doi.org/ 10.3390/rs13173542, 2021.

de Leeuw, G., Fan, C, Li, Z., Dong, J., Li, Y., Ou, Y., and Zhu, S. (2022). Spatiotemporal variation and provincial scale differences of the AOD across China during 2000–2021. Atmospheric Pollution Research 13 (2022) 101359 (14 pp). https://doi.org/10.1016/j.apr.2022.101359.

de Leeuw, G., Kang, H., Fan, C., Li, Z., Fang, C., Zhang, Y. (2023). Meteorological and anthropogenic contributions to changes in the Aerosol Optical Depth (AOD) over China during the last decade. Atm. Env., 301, 119676. https://doi.org/10.1016/j.atmosenv.2023.119676.

Ekman, A. M. L., Eva Nygren, Alejandro Baró Pérez, Matthias Schwarz, Gunilla Svensson, Nicolas Bellouin.: Influence of horizontal resolution and complexity of aerosol–cloud interactions on marine stratocumulus and stratocumulus-to-cumulus transition in HadGEM3-GC3.1, Quart. J Royal Met Soc., 149, 755, 2049-2066, https://doi.org/10.1002/qj.4494, 2023.

Fan J, Wang Y, Rosenfeld D, et al.: Review of aerosol-cloud interactions: Mechanisms, significance, and challenges. Journal of the Atmospheric Sciences,73(11): 4221-4252, 2016.

Fan, J., Zhang, Y., Li, Z., Yan, H., Prabhakaran, T., Rosenfeld, D., & Khain, A.: Unveiling aerosol impacts on deep convective clouds: Scientific concept, modeling, observational analysis, and future direction, Journal of Geophysical Research: Atmospheres, 130, e2024JD041931. https://doi.org/10.1029/2024JD041931, 2025.

Feingold, G., Remer, L. A., Ramaprasad, J., Kaufman, Y. J.: Analysis of smoke impact on clouds in Brazilian biomass burning regions: an extension of Twomey's approach, J. Geophys. Res., 106 (D19), 22907-22922, 2001.

Feingold, G. Modeling of the first indirect effect: analysis of measurement requirements, Geophys. Res. Lett., 30, 1997, doi:10.1029/2003GL017967, 2003.

Feingold, G., Goren, T., and Yamaguchi, T.: Quantifying albedo susceptibility biases in shallow clouds, Atmos. Chem. Phys., 22, 3303–3319, https://doi.org/10.5194/acp-22-3303-2022, 2022.

Grandey, B.S., Stier, P.: A critical look at spatial scale choices in satellite-based aerosol indirect effect studies. Atmos. Chem. Phys., 10, 11459-11470, 2010.

Gryspeerdt, E., Stier, P., and Partridge, D. G.: Satellite observations of cloud regime development: the role of aerosol processes, Atmos. Chem. Phys., 14, 1141-1158, doi:10.5194/acp-14-1141-2014, 2014.

Gryspeerdt, E., Povey, A. C., Grainger, R. G., Hasekamp, O., Hsu, N. C., Mulcahy, J. P., Sayer, A. M., and Sorooshian, A.: Uncertainty in aerosol–cloud radiative forcing is driven by clean conditions, Atmos. Chem. Phys., 23, 4115-4122, https://doi.org/10.5194/acp-23-4115-2023, 2023.

Gryspeerdt, E., McCoy, D. T., Crosbie, E., Moore, R. H., Nott, G. J., Painemal, D., Small-Griswold, J., Sorooshian, A., and Ziemba, L.: The impact of sampling strategy on the cloud droplet number concentration estimated from satellite data, Atmos. Meas. Tech., 15, 3875–3892, 2022, https://doi.org/10.5194/amt-15-3875-2022, 2022.

Glotfelty, T., Kiran Alapaty, Jian He, Patrick Hawbecker, Xiaoliang Song, and Guang Zhang. Studying Scale Dependency of Aerosol–Cloud Interactions Using Multiscale Cloud Formulations, 77, 11, 2020.

Grosvenor, D. P., Sourdeval, O., Zuidema, P., Ackerman, A., Alexandrov, M. D., Bennartz, R., Boers, R., Cairns, B., Chiu, J. C., Christensen, M., Deneke, H., Diamond, M., Feingold, G., Fridlind, A., Hünerbein, A., Knist, C., Kollias, P., Marshak, A., McCoy, D., Merk, D., Painemal, D., Rausch, J., Rosenfeld, D., Russchenberg, H., Seifert, P., Sinclair, K., Stier, P., Diedenhoven, B. V., Wendisch, M., Werner, F., Wood, R., Zhang, Z., and Quaas, J.: Remote sensing of droplet number concentration in warm clouds: A review of the current state of knowledge and perspectives, Rev. Geophys., 56, 409–453, https://doi.org/10.1029/2017RG000593, 2018.

Han, X., Zhao, B., Lin, Y., Chen,Q., Shi, H., Jiang, Z., et al.: Type-dependent impact of aerosols on precipitation associated with deep convective cloud over East Asia, Journal of Geophysical Research: Atmospheres,127, e2021JD036127. ttps://doi.org/10.1029/2021JD036127, 2022.

Hassan, T., Zhang, K., Li, J., Singh, B., Zhang, S., Wang, H., and Ma, P.: Impacts of spatial heterogeneity of anthropogenic aerosol emissions in a regionally refined global aerosol–climate model, Geosci. Model Dev., 17, 3507-3532, 2024.

Huang, R. J., Zhang, Y. L., Bozzetti, C., et al. High secondary aerosol contribution to particulate pollution during haze events in China, Nature, 514, 218–222, 2014.

Jia, H. L., Ma, X. Y., Quaas, J., Yin, Y., Qiu, T.: Is positive correlation between cloud droplet effective radius and aerosol optical depth over land due to retrieval artifacts or real physical processes? Atmospheric Chemistry and Physics, 19, 13, 8879-8896, 2019.

Jia, H., Quaas, J., Gryspeerdt, E., Böhm, C., & Sourdeval, O.: Addressing the difficulties in quantifying droplet number response to aerosol from satellite observations, Atmospheric Chemistry and Physics, 22(11), 7353–7372. https://doi.org/10.5194/acp-22-7353-2022, 2022.

Jones, T. A., Christopher, S. A., & Quaas, J.: A six year satellite-based assessment of the regional variations in aerosol indirect effects. Atmospheric Chemistry and Physics, 9, 4091, 2009.

Koren, I., Kaufman, Y. J., Rosenfeld, D., Remer, L. A., Rudich, Y.: Aerosol invigoration and restructuring of Atlantic convective clouds. Geophys. Res. Lett., 32 (14), L14828, 2005.

Kaufman, Y.J. and Fraser, R.S.: The effect of smoke particles on clouds and climate forcing. Science, 1997. 277(5332): p. 1636-1639.

Kaufman, Y. J., Remer, L., Tanr´e, D., Li, R., Kleidman, R., Mattoo, S., Levy, R., Eck, T., Holben, B., Ichoku, C., Martins, J., and Koren, I.: A critical examination of the residual cloud contamination and diurnal sampling effects on MODIS estimates of aerosol over ocean, IEEE Trans. Geosci. Remote Sens., 43, 2886–2897, 2005.

Kaufman, Y.J., Remer, L.A., Tanré, D., Li, R.R., Kleidman, R., Mattoo, S., Levy, R.C., Eck, T.F., Holben, B.N., Ichoku, C., Member, IEEE, Martins, J.V., and Koren, I.: A Critical Examination of the Residual

Cloud Contamination and Diurnal Sampling Effects on MODIS Estimates of Aerosol Over Ocean, IEEE TRANSACTIONS ON GEOSCIENCE AND REMOTE SENSING, 43, 12, 2005.

Kim, S. W., S. C. Yoon, J. Y. Kim, and S. Y. Kim (2007), Seasonal and monthly variations of columnar aerosol optical properties over East Asia determined from multi-year MODIS, LIDAR, and AERONET Sun/sky radiometer measurements, Atmos. Environ., 41(8), 1634–1651, doi:10.1016/j.atmosenv.2006.10.044.

King, M. D., Tsay, S. C., Platnick, S. E., Wang, M., and Liou, K. N.: Cloud Retrieval Algorithms for MODIS: Optical Thickness, Effective Particle Radius, and Thermodynamic Phase, MODIS Algorithm Theoretical Basis Document, available at: http://eospso.nasa.gov/sites/default/files/atbd/atbd_mod05.pdf, 1997.

King, M. D., Menzel, W. P., Kaufman, Y. J., Tanré, D., Gao, B. C., Platnick, S., Ackerman, S. A., Remer, L. A., Pincus, R., and Hubanks, P. A.: Cloud and aerosol properties, precipitable water, and profiles of temperature and water vapor from MODIS, IEEE T. Geosci. Remote, 41, 442–458, doi:10.1109/TGRS.2002.808226, 2003.

Lebsock, M., Morrison, H., Gettelman, A.: Microphysical implications of cloud-precipitation covariance derived from satellite remote sensing. Journal of Geophysical Research: Atmosphere, 118, 6521-6533, 2013.

Levy, R. C., Mattoo, S., Munchak, L. A., Remer, L. A., Sayer, A. M., Patadia, F., and Hsu, N. C.: The Collection 6 MODIS aerosol products over land and ocean, Atmos. Meas. Tech., 6, 2989-3034, https://doi.org/10.5194/amt-6-2989-2013, 2013.

Levy, R. C., Remer, L. A., Kleidman, R. G., Mattoo, S., Ichoku, C., Kahn, R., and Eck, T. F.: Global evaluation of the Collection 5 MODIS dark-target aerosol products over land, Atmos. Chem. Phys., 10, 10399–10420, doi:10.5194/acp-10-10399-2010, 2010.

Lee, S. S., Donner, L. J., Phillips, V. T. J. Impacts of aerosol chemical composition on microphysics and precipitation in deep convection, Atmospheric Research, 94, 220–237, 2009.

Lee, H.-H., Zheng, X., Qiu, S., and Wang, Y.: Numerical case study of the aerosol–cloud interactions in warm boundary layer clouds over the eastern North Atlantic with an interactive chemistry module, Atmos. Chem. Phys., 25, 6069–6091, https://doi.org/10.5194/acp-25-6069-2025, 2025.

Leung, G. R., Saleeby, S. M., Sokolowsky, G. A., Freeman, S. W., and van den Heever, S. C.: Aerosol–cloud impacts on aerosol detrainment and rainout in shallow maritime tropical clouds, Atmos. Chem. Phys., 23, 5263–5278, https://doi.org/10.5194/acp-23-5263-2023, 2023.

Li, G. H., Wang, Y., Zhang, R. Y.: Implementation of a two-moment bulk microphysics scheme to the WRF model to investigate aerosol-cloud interaction, Journal of Geophysical Research-Atmospheres, 113, D15, https://doi.org/10.1029/2007JD009361, 2008.

Li, Z., et al.: Aerosol and monsoon climate interactions over Asia, Rev. Geophys., 54, 866–929, doi:10.1002/2015RG000500, 2016.

Li, Y., Liu, X., and Cai, H.: Numerical simulation of aerosol concentration effects on cloud droplet size spectrum evolutions of warm stratiform clouds in Jiangxi, China, Atmos. Chem. Phys., 24, 13525–13540, https://doi.org/10.5194/acp-24-13525-2024, 2024.

Liu, Y., Lin, T., Zhang, J., Wang, F., Huang, Y., Wu, X., Ye, H., Zhang, G., Cao, X., and de Leeuw, G.: Opposite effects of aerosols and meteorological parameters on warm clouds in two contrasting regions over eastern China, Atmos. Chem. Phys., 24, 4651–4673, https://doi.org/10.5194/acp-24-4651-2024, 2024.

Liu, Q., Duan, S. Y., He, Q. S., Chen, Y. H., Zhang, H., Cheng, N. X., Huang, Y. W., Chen, B., Zhan, Q. Y., Li, J. Z.: The variability of warm cloud droplet radius induced by aerosols and water vapor in Shanghai from MODIS observations, Atmospheric Research, 253, 105470, 2021.

Liu, Q., Shen, X., Li, L., et al. Impacts of Aerosol Chemical Composition on Cloud Condensation Nuclei (CCN) Activity during Wintertime in Beijing, China. Remote Sens., 15, 4119, 2023.

Liu, T. Q., Liu, Q., Chen, Y. H., Wang, W. C., Zhang, H., Li, D., Sheng, J.: Effect of aerosols on the macro- and micro-physical properties of warm clouds in the Beijing-Tianjin-Heibei region. Science of the Total Environmen, 720, 137618, 2020.

Liu, Y., Zhang, J., Zhou, P., Lin, T., Hong, J., Shi, L., Yao, F., Wu, J., Guo, H., and de Leeuw, G.: Satellite-based estimate of the variability of warm cloud properties associated with aerosol and meteorological conditions, Atmos. Chem. Phys., 18, 18187-18202, https://doi.org/10.5194/acp-18-18187-2018, 2018.

Liu, Y., de Leeuw, G., Kerminen, V.-M., Zhang, J., Zhou, P., Nie, W., Qi, X., Hong, J., Wang, Y., Ding, A., Guo, H., Krüger, O., Kulmala, M., and Petäjä, T.: Analysis of aerosol effects on warm clouds over the Yangtze River Delta from multi-sensor satellite observations, Atmos. Chem. Phys., 17, 5623-5641, https://doi.org/10.5194/acp-17-5623-2017, 2017.

Liu, Z., Vaughan, M., Winker, D., Kittaka, C., Getzewich, B., Kuehn, R., Omar, A.,Powell, K., Trepte, C., and Hostetler, C.:The CALIPSO lidar cloud and aerosol discrimination: Version 2 algorithm and initial assessment of performance, J. Atmos. Ocean. Tech., 26, 1198–1213, 2009.

Ma, X., Jia, H., Yu, F., and Quaas, J.: Opposite aerosol index-cloud droplet effective radius correlations over major industrial regions and their adjacent oceans, Geophys. Res. Lett., 45, 5771–5778, https://doi.org/10.1029/2018GL077562, 2018.

Ma, P.-L., P. J. Rasch, M. Wang, H. Wang, S. J. Ghan, R. C. Easter, W. I. Gustafson Jr., X. Liu, Y. Zhang, and H.-Y. Ma (2015), How does increasing horizontal resolution in a global climate model improve the simulation of aerosol-cloud interactions?, Geophys. Res. Lett., 42, 5058–5065, doi:10.1002/2015GL064183.

Marchant, B., et al.: MODIS Collection 6 shortwave-derived cloud phase classification algorithm and comparisons with CALIOP, Atmos. Meas. Tech. Discuss., 8, 11893–11924, 2015.

Matheson, M. A., Coakley Jr., J. A., and Tahnk, W. R.: Aerosol and cloud property from relationships for summer stratiform clouds in the northeastern Atlantic from advanced very high resolution radiometer observations, J. Geophys. Res., 110, D24204, doi:10.1029/2005JD006165, 2005.

McComiskey, A., & Feingold, G: The scale problem in quantifying aerosol indirect effects. Atmospheric Chemistry and Physics, 12, 1031. https://doi.org/10.5194/acp-12-1031-2012, 2012.

Meskhidze, N., Nenes, A.: Effects of ocean ecosystem on marine aerosol-cloud interaction. Adv. Meteorol, doi:10.1155/2010/239808, 2010.

Mohebalhojeh, M., Frederick, S., Riemer, N., & West, M. (2026). A Metric for Quantifying Spatial Heterogeneity in Gridded Atmospheric Fields. Earth and Space Science (preprint).

Murray-Watson, R. J. and Gryspeerdt, E.: Stability-dependent increases in liquid water with droplet number in the Arctic, Atmos. Chem. Phys., 22, 5743–5756, https://doi.org/10.5194/acp-22-5743-2022, 2022.

McComiskey, A., G. Feingold, A. S. Frisch, D. D. Turner, M. A. Miller, J. C. Chiu, Q. Min, and J. A. Ogren (2009), Anassessment of aerosol-cloud interactions in marine stratus clouds based on surface remote sensing, J. Geophys. Res., 114, D09203,doi:10.1029/2008JD011006.

Platnick, S., et al., MODIS Cloud optical properties: User guide for the Collection 6/6.1 level-2 MOD06/MYD06 product and associated level-3 data sets. v1.1, July 2018.

Proestakis, E., Amiridis, V., Marinou, E., Georgoulias, A. K., Solomos, S., Kazadzis, S., Chimot, J., Che, H., Alexandri, G., Binietoglou, I., Daskalopoulou, V., Kourtidis, K. A., de Leeuw, G., and van der A, R. J.: Nine-year spatial and temporal evolution of desert dust aerosols over South and East Asia as revealed by CALIOP, Atmos. Chem. Phys., 18, 1337-1362, https://doi.org/10.5194/acp-18-1337-2018, 2018.

Possner A., Zubler, E. M., Lohmann, U., and Schär, C.: The resolution dependence of cloud effects and ship-induced aerosol-cloud interactions in marine stratocumulus, J. Geophys. Res. Atmos., 121, 4810–4829, doi:10.1002/2015JD024685, 2016.

Pandey, S. K., Vinoj, V., Panwar, A.: The short-term variability of aerosols and their impact on cloud properties and radiative effect over the Indo-Gangetic Plain. Atmospheric Pollution Research, 11, 630-638, 2020.

Platnick, S., Meyer, K. G., King, M. D., Wind, G., Amarasinghe, N., Marchant, B., Arnold, G. T., Zhang, Z., Hubanks, P. A., Holz, R. E., Yang, P., Ridgway, W. L., Riedi, J.: The MODIS cloud optical and microphysical products: Collection 6 updates and examples from Terra and Aqua. IEEE Trans Geosci Remote Sens. Jan;55(1):502-525. doi: 10.1109/TGRS.2016.2610522, 2017.

Quaas, J., Boucher, O., Bellouin, N., Kinne, S.: Satellite-based estimate of the direct and indirect aerosol climate forcing, J. Geophys. Res., 113, D05204, doi:10.1029/2007JD008962, 2008.

Quaas, J., Stevens, B., Stier, P., and Lohmann, U.: Interpreting the cloud cover – aerosol optical depth relationship found in satellite data using a general circulation model, Atmos. Chem. Phys., 10, 6129-6135, https://doi.org/10.5194/acp-10-6129-2010, 2010.

Quaas, J., Boucher, O., and Lohmann, U.: Constraining the total aerosol indirect effect in the LMDZ and ECHAM4 GCMs using MODIS satellite data, Atmos. Chem. Phys., 6, 947–955, https://doi.org/10.5194/acp-6-947-2006, 2006.

Quaas, J., Ming, Y., Menon, S., Takemura, T., Wang, M., Penner, J. E., Gettelman, A., Lohmann, U., Bellouin, N., Boucher, O., Sayer, A. M., Thomas, G. E., McComiskey, A., Feingold, G., Hoose, C., Kristjánsson, J. E., Liu, X., Balkanski, Y., Donner, L. J., Ginoux, P. A., Stier, P., Grandey, B., Feichter, J., Sednev, I., Bauer, S. E., Koch, D., Grainger, R. G., Kirkevåg, A., Iversen, T., Seland, Ø., Easter, R., Ghan, S. J., Rasch, P. J., Morrison, H., Lamarque, J.-F., Iacono, M. J., Kinne, S., and Schulz, M.: Aerosol indirect effects – general circulation model intercomparison and evaluation with satellite data, Atmos. Chem. Phys., 9, 8697–8717, https://doi.org/10.5194/acp-9-8697-2009, 2009.

Rao, S., Dey, S.: Consistent signal of aerosol indirect and semi-direct effect on water clouds in the oceanic regions adjacent to the Indian subcontinent. Atmospheric Research, 232, 2020.

Remer, L. A., Kaufman, Y. J., Tanre, D., Mattoo, S., Chu, D. A., Martins, J. V., Li, R. R., Ichoku, C., Levy, R. C., Kleidman, R. G., Eck, T. F., Vermote, E., and Holben, B. N.: The MODIS aerosol algorithm, products, and validation, J. Atmos. Sci., 62, 947–973, https://doi.org/10.1175/JAS3385.1, 2005.

Rosenfeld, D., Zhu, Y. N., Wang, M. H., Zheng, Y. T., Goren, T., Yu, S. C.: Aerosol-driven droplet concentrations dominate coverage and water of oceanic low-level clouds, Science, 363, 6427, 2019.

Sarna, K. and Russchenberg, H. W. J.: Ground-based remote sensing scheme for monitoring aerosol–cloud interactions, Atmos. Meas. Tech., 9, 1039–1050, https://doi.org/10.5194/amt-9-1039-2016, 2016.

Saponaro, G., Kolmonen, P., Sogacheva, L., Rodriguez, E., Virtanen, T., de Leeus, G.: Estimates of the aerosol indirect effect over the Baltic Sea region derived from 12 years of MODIS observations, Atmos. Chem. Phys., 17, 3133-3143, 2017.

Stephens, G., Vane, D. G., Boain, R. J., Mace, G. G., Sassen, K., Wang, Z., Illingworth, A. J., O'Connor, E. J., Rossow, W. B., Durden, S. L., Miller, S. D., Austin, R. T., Benedetti, A., and Mitrescu, C.: The CloudSat Science Team: The CloudSat mission and the A-Train, B. Am. Meteorol. Soc., 83, 1771–1790, 2002.

Sourdeval, O., Laurent C.-Labonnote, Anthony J. Baran, Johannes Mülmenstädt, Gérard Brogniez.: A methodology for simultaneous retrieval of ice and liquid water cloud properties. Part 2: Near-global retrievals and evaluation against A-Train products, Quarterly Journal of the Royal Meteorological Society, 142, 701, 3063-3081, 2016.

Sundström, A.-M., Kolmonen, P., Sogacheva, L., and de Leeuw, D.: Aerosol retrievals over China with the AATSR dual view algorithm, Remote Sens. Environ., 116, 189–198, 2012.

Theodore L. Anderson, Robert J. Charlson, David M. Winker, John A. Ogren, and Kim Holmén.: Mesoscale Variations of Tropospheric Aerosols, Journal of the Atmospheric Sciences, 60, 1, https://doi.org/10.1175/1520-0469(2003)060<0119:MVOTA>2.0.CO;2, 2003.

Tang, J., Wang, P., Mickley, L. J., Xia, X., Liao, H., Yue, X., et al.: Positive relationship between liquid cloud droplet effective radius and aerosol optical depth over Eastern China from satellite data. Atmospheric Environment, 84, 244-253. https://doi.org/10.1016/j.atmosenv.2013.08.024, 2014.

Tao, W. K., Chen, J. P., Li, Z., Wang, C. E., Zhang, C. D.: Impact of aerosols on convective clouds and precipitation, Reviews of Geophysics, 50(2), 2012.

Twomey, S. Pollution and the planetary albedo, Atmos. Environ., 1974, 41, 120-125.

Twomey, S.: The influence of pollution on the shortwave albedo of clouds, J. Atmos. Sci. 34(7), 1149-1152, 1977.

Wang, F., Guo, J., Zhang, J., Wu, Y., Zhang, X., Deng, M., and Li, X.: Satellite observed aerosol-induced variability in warm cloud properties under different meteorological conditions over eastern China, Atmos. Environ., 84, 122–132, 2014.

Wang, F., Guo, J., Zhang, J., Wu, Y., Zhang, X., Deng, M., Li, X.: Satellite observed aerosol-induced variability in warm cloud properties under different meteorological conditions over eastern China, Atmos. Environ., 84, 122-132, 2014.

Wang, Y., Wang, Y., Song, X., Shang, Y., Zhou, Y., Huang, X., Li, Z.: The impact of particulate pollution control on aerosol hygroscopicity and CCN activity in North China, Environmental Research Letters, 18, 074028, 2023.

Winker, D. M., Pelon, J. R., and McCormick, M. P.: The CALIPSO mission: Spacebornelidar for observation of aerosols and clouds, Proc. SPIE, Lidar Remote Sensing for Industry and Environment Monitoring III, 4893, doi:10.1117/12.466539, 2003.

Winker, D. M., Hunt, W. H., and McGill, M. J.: Initial performance assessment of CALIOP, Geophys. Res. Lett., 34, L19803, doi:10.1029/ 2007GL030135, 2007.

Winker, D. M., Vaughan, M. A., Omar, A., Hu, Y., Powell, K. A., Liu, Z. Y., Hunt, W. H., Young, S. A.: Overview of the CALIPSO Mission and CALIOP Data Processing Algorithms, Journal of Atmospheric and Oceanic Technology, 26 (11), 2310-2323, 2009. doi:10.1175/2009JTECHA1281.1.

Winker, D. M., Pelon, J., Coakley Jr, J. A., Ackerman, S. A., Charlson, R. J., Colarco, P. R., Flamant, P., Fu, Q., Hoff, R. M., Kittaka, C., Kubar, T. L., Le Treut, H., Mccormick, M. P., Mégie, G., Poole, L., Powell, K., Trepte, C., Vaughan, M. A., and Wielicki, B. A.: The CALIPSO Mission. Bulletin of American Meteorological Society, 91(9), 1211-1230, 2010.

Wang, F., Guo, J., Zhang, J., Huang, J., Min, M., Chen, T., Liu, H., Deng, M., Li, X.: Multi-sensor quantification of aerosol-induced variability in warm clouds over eastern China, Atmos. Environ., 113: 1-9, 2015. http://dx.doi.org/10.1016/j.atmosenv.2015.04.063.

Yuan, T., Li, Z., Zhang, R., and Fan, J.: Increase of cloud droplet size with aerosol optical depth: an observation and modeling study, J. Geophys. Res., 113, D04201, doi:10.1029/2007JD008632, 2008.

Zhang, L., Li, J., Li, J., Li, R., Zhang, W., Lei, M., et al.: Studying the impacts of meteorological factors on distribution of cloud horizontal scales based on active satellite, Journal of Geophysical Research: Atmospheres, 129, e2024JD041844, https://doi.org/10.1029/2024JD041844, 2024.

Zhang, Q., Meng, J., Quan, J., et al. Impact of aerosol composition on cloud condensation nuclei activity, Atmos. Chem. Phys., 12, 3783–3790, 2012.

Zhao, J., Ma, X., Quaas, J., and Yang, T.: How meteorological conditions influence aerosol-cloud interactions under different pollution regimes, Atmos. Chem. Phys., 25, 17701–17723, https://doi.org/10.5194/acp-25-17701-2025, 2025.

Zheng, B., Tong, D., Li, M., Liu, F., Hong, C., Geng, G., Li, H., Li, X., Peng, L., Qi, J., Yan, L., Zhang, Y., Zhao, H., Zheng, Y., He, K., and Zhang, Q.: Trends in China's anthropogenic emissions since 2010 as the consequence of clean air actions, Atmos. Chem. Phys., 18, 14095–14111, https://doi.org/10.5194/acp-18-14095-2018, 2018.

Zheng, X., Dong, X., Xi, B., Logan, T., and Wang, Y.: Distinctive aerosol–cloud–precipitation interactions in marine boundary layer clouds from the ACE-ENA and SOCRATES aircraft field campaigns, Atmos. Chem. Phys., 24, 10323–10347, https://doi.org/10.5194/acp-24-10323-2024, 2024.

Zheng, X., Xi, B., Dong, X., Logan, T., Wang, Y., and Wu, P.: Investigation of aerosol–cloud interactions under different absorptive aerosol regimes using Atmospheric Radiation Measurement (ARM) southern Great Plains (SGP) ground-based measurements, Atmos. Chem. Phys., 20, 3483–3501, https://doi.org/10.5194/acp-20-3483-2020, 2020.